Astronomy & Astrophysics

A multifrequency study of sub-parsec jets with the Event Horizon Telescope

Jan Röder[1,2],[⋆], Maciek Wielgus[2,1], Andrei P. Lobanov[1], Thomas P. Krichbaum[1], Dhanya G. Nair[3,1],
Sang-Sung Lee[4], Eduardo Ros[1], Vincent L. Fish[5], Lindy Blackburn[6,7], Chi-kwan Chan[8,9,10],
Sara Issaoun[7,11], Michael Janssen[12,1], Michael D. Johnson[6,7], Sheperd S. Doeleman[6,7],
Geoffrey C. Bower[13,14], Geoffrey B. Crew[5], Remo P. J. Tilanus[8,12,15,16], Tuomas Savolainen[17,18,1],
C. M. Violette Impellizzeri[15,19], Antxon Alberdi[2], Anne-Kathrin Baczko[20,1], José L. Gómez[2],
Ru-Sen Lu[21,53,1], Georgios F. Paraschos[1], Efthalia Traianou[2,1], Ciriaco Goddi[22,23,24,25], Daewon Kim[1],
Mikhail Lisakov[26], Yuri Y. Kovalev[1,6], Petr A. Voitsik[27], Kirill V. Sokolovsky[28], Kazunori Akiyama[5,29,6],
Ezequiel Albentosa-Ruíz[30], Walter Alef[1], Juan Carlos Algaba[31], Richard Anantua[6,7,32], Keiichi Asada[33],
Rebecca Azulay[30,34,1], Uwe Bach[1], David Ball[8], Mislav Baloković[35], Bidisha Bandyopadhyay[3],
John Barrett[5], Michi Bauböck[36], Bradford A. Benson[37,38], Dan Bintley[39,40], Raymond Blundell[7],
Katherine L. Bouman[41], Michael Bremer[42], Christiaan D. Brinkerink[12], Roger Brissenden[6,7], Silke Britzen[1],
Avery E. Broderick[43,44,45], Dominique Broguiere[42], Thomas Bronzwaer[12], Sandra Bustamante[46],
Do-Young Byun[4,47], John E. Carlstrom[48,38,49,50], Chiara Ceccobello[20], Andrew Chael[51],
Dominic O. Chang[6,7], Koushik Chatterjee[6,7], Shami Chatterjee[52], Ming-Tang Chen[13], Yongjun Chen[21,53],
Xiaopeng Cheng[4], Ilje Cho[2,4,54], Pierre Christian[55], Nicholas S. Conroy[28,7], John E. Conway[20],
James M. Cordes[52], Thomas M. Crawford[38,48], Alejandro Cruz-Osorio[56,57], Yuzhu Cui[58,59],
Brandon Curd[32,6,7], Rohan Dahale[2], Jordy Davelaar[60,61,12], Mariafelicia De Laurentis[62,57,63],
Roger Deane[64,65,66], Jessica Dempsey[39,40,67], Gregory Desvignes[1,68], Jason Dexter[69], Vedant Dhruv[36],
Indu K. Dihingia[59], Sean Taylor Dougall[8], Sergio A. Dzib[42,1], Ralph P. Eatough[70,1], Razieh Emami[7],
Heino Falcke[12], Joseph Farah[71,72], Edward Fomalont[19], H. Alyson Ford[8], Marianna Foschi[2],
Raquel Fraga-Encinas[12], William T. Freeman[73,74], Per Friberg[39,40], Christian M. Fromm[75,57,1],
Antonio Fuentes[2], Peter Galison[6,76,77], Charles F. Gammie[36,28,78], Roberto García[42], Olivier Gentaz[42],
Boris Georgiev[8], Roman Gold[79,80,81], Arturo I. Gómez-Ruiz[82,83], Minfeng Gu[21,84], Mark Gurwell[7],
Kazuhiro Hada[85,86], Daryl Haggard[87,88], Kari Haworth[7], Michael H. Hecht[5], Ronald Hesper[89],
Dirk Heumann[8], Luis C. Ho[90,91], Paul Ho[33,40,39], Mareki Honma[85,86,92], Chih-Wei L. Huang[33],
Lei Huang[21,84], David H. Hughes[82], Shiro Ikeda[29,93,94,95], Makoto Inoue[33], David J. James[96,97],
Buell T. Jannuzi[8], Britton Jeter[33], Wu Jiang[21], Alejandra Jiménez-Rosales[12], Svetlana Jorstad[98],
Abhishek V. Joshi[36], Taehyun Jung[4,47], Mansour Karami[43,44], Ramesh Karuppusamy[1],
Tomohisa Kawashima[99], Garrett K. Keating[7], Mark Kettenis[100], Dong-Jin Kim[1], Jae-Young Kim[101,1],
Jongsoo Kim[4], Junhan Kim[102], Motoki Kino[29,103], Jun Yi Koay[33], Prashant Kocherlakota[6,7,57],
Yutaro Kofuji[85,92], Shoko Koyama[104,33], Carsten Kramer[42], Joana A. Kramer[1], Michael Kramer[1],
Cheng-Yu Kuo[105,33], Noemi La Bella[12], Tod R. Lauer[106], Daeyoung Lee[36], Po Kin Leung[107],
Aviad Levis[41], Zhiyuan Li[108,109], Rocco Lico[110,2], Greg Lindahl[7], Michael Lindqvist[20], Jun Liu[1],
Kuo Liu[1], Elisabetta Liuzzo[111], Wen-Ping Lo[33,112], Laurent Loinard[113,6,114], Colin J. Lonsdale[5],
Amy E. Lowitz[8], Nicholas R. MacDonald[1], Jirong Mao[115,116,117], Nicola Marchili[111,1], Sera Markoff[118,119],
Daniel P. Marrone[8], Alan P. Marscher[98], Iván Martí-Vidal[30,34], Satoki Matsushita[33], Lynn D. Matthews[5],
Lia Medeiros[120,11], Karl M. Menten[1],[⋆⋆], Daniel Michalik[121,122], Izumi Mizuno[39,40], Yosuke Mizuno[59,123,57],
James M. Moran[6,7], Kotaro Moriyama[57,5,85], Monika Moscibrodzka[12], Wanga Mulaudzi[118],
Cornelia Müller[1,12], Hendrik Müller[124], Alejandro Mus[23,24], Gibwa Musoke[118,12], Ioannis Myserlis[125],
Andrew Nadolski[28], Hiroshi Nagai[29,86], Neil M. Nagar[3], Masanori Nakamura[126,33], Gopal Narayanan[46],
Iniyan Natarajan[7,6], Antonios Nathanail[127,57], Santiago Navarro Fuentes[125], Joey Neilsen[128], Roberto Neri[42],

---

⋆ Corresponding author; jroeder.astro@gmail.com

⋆⋆ Deceased.

Chunchong Ni[44,45,43], Aristeidis Noutsos[1], Michael A. Nowak[129], Junghwan Oh[100], Hiroki Okino[85,92],
Héctor R. Olivares Sánchez[130], Gisela N. Ortiz-León[82,1], Tomoaki Oyama[85], Feryal Özel[131],
Daniel C. M. Palumbo[6,7], Jongho Park[132,33], Harriet Parsons[39,40], Nimesh Patel[7], Ue-Li Pen[33,43,133,134,135],
Dominic W. Pesce[7,6], Vincent Piétu[42], Richard Plambeck[136], Aleksandar PopStefanija[46], Oliver Porth[118,57],
Felix M. Pötzl[137], Ben Prather[36], Jorge A. Preciado-López[43], Giacomo Principe[138,139,110],
Dimitrios Psaltis[131], Hung-Yi Pu[140,141,33], Venkatessh Ramakrishnan[3,142,18], Ramprasad Rao[7],
Mark G. Rawlings[143,39,40], Angelo Ricarte[6,7], Bart Ripperda[133,144,134,43], Freek Roelofs[12], Alan Rogers[5],
Cristina Romero-Cañizales[33], Arash Roshanineshat[8], Helge Rottmann[1], Alan L. Roy[1], Ignacio Ruiz[125],
Chet Ruszczyk[5], Kazi L. J. Rygl[111], Salvador Sánchez[125], David Sánchez-Argüelles[82,83],
Miguel Sánchez-Portal[125], Mahito Sasada[145,85,146], Kaushik Satapathy[8], F. Peter Schloerb[46],
Jonathan Schonfeld[7], Karl-Friedrich Schuster[147], Lijing Shao[91,1], Zhiqiang Shen[21,53], Des Small[100],
Bong Won Sohn[4,47,54], Jason SooHoo[5], León David Sosapanta Salas[118], Kamal Souccar[46],
Joshua S. Stanway[148], He Sun[149,150], Fumie Tazaki[85], Alexandra J. Tetarenko[151], Paul Tiede[7,6],
Michael Titus[5], Pablo Torne[125,1], Teresa Toscano[2], Tyler Trent[8], Sascha Trippe[152], Matthew Turk[28],
Ilse van Bemmel[67], Huib J. van Langevelde[100,15,153], Daniel R. van Rossum[12], Jesse Vos[12], Jan Wagner[1],
Derek Ward-Thompson[148], John Wardle[154], Jasmin E. Washington[8], Jonathan Weintroub[6,7],
Robert Wharton[1], Kaj Wiik[18,142,155], Gunther Witzel[1], Michael F. Wondrak[12,156], George N. Wong[157,51],
Qingwen Wu[158], Nitika Yadlapalli[41], Paul Yamaguchi[7], Aristomenis Yfantis[12], Doosoo Yoon[118],
André Young[12], Ken Young[7], Ziri Younsi[159,57], Wei Yu[7], Feng Yuan[160], Ye-Fei Yuan[161],
J. Anton Zensus[1], Shuo Zhang[162], Guang-Yao Zhao[2,1], Shan-Shan Zhao[21]

(Affiliations can be found after the references)

ABSTRACT

Context. The 2017 observing campaign of the Event Horizon Telescope (EHT) delivered the first very long baseline interferometry (VLBI) images at the observing frequency of 230 GHz, leading to a number of unique studies on black holes and relativistic jets from active galactic nuclei (AGN). In total, eighteen sources were observed, including the main science targets, Sgr A* and M 87, and various calibrators. Sixteen sources were AGN.
Aims. We investigated the morphology of the sixteen AGN in the EHT 2017 data set, focusing on the properties of the VLBI cores: size, flux density, and brightness temperature. We studied their dependence on the observing frequency in order to compare it with the Blandford-Königl (BK) jet model. In particular, we aimed to study the signatures of jet acceleration and magnetic energy conversion.
Methods. We modeled the source structure of seven AGN in the EHT 2017 data set using linearly polarized circular Gaussian components (1749+096, 1055+018, BL Lac, J0132–1654, J0006–0623, CTA 102, and 3C 454.3) and collected results for the other nine AGN from dedicated EHT publications, complemented by lower frequency data in the 2–86 GHz range. Combining these data into a multifrequency EHT+ data set, we studied the dependences of the VLBI core component flux density, size, and brightness temperature on the frequency measured in the AGN host frame (and hence on the distance from the central black hole), characterizing them with power law fits. We compared the observations with the BK jet model and estimated the magnetic field strength dependence on the distance from the central black hole.
Results. Our observations spanning event horizon to parsec scales indicate a deviation from the standard BK model, particularly in the decrease of the brightness temperature with the observing frequency. Only some of the discrepancies may be alleviated by tweaking the model parameters or the jet collimation profile. Either bulk acceleration of the jet material, energy transfer from the magnetic field to the particles, or both are required to explain the observations. For our sample, we estimate a general radial dependence of the Doppler factor $\delta \propto r^{0.5}$. This interpretation is consistent with a magnetically accelerated sub-parsec jet. We also estimate a steep decrease of the magnetic field strength with radius $B \propto r^{-3}$, hinting at jet acceleration or efficient magnetic energy dissipation.

Key words. techniques: interferometric – galaxies: active – galaxies: jets – galaxies: nuclei – quasars: general – quasars: supermassive black holes

1. Introduction

Some supermassive black holes (SMBHs) in the centers of galaxies power highly collimated outflows reaching thousands of parsecs into interstellar, and sometimes intergalactic space: relativistic jets. These jets are formed and accelerated in a compact region close to the black hole, the active galactic nucleus (AGN). The detailed physics governing this region, such as the mechanisms for jet formation, collimation and acceleration, as well as the role of magnetic fields, are subjects of extensive active work (see, e.g., Blandford et al. 2019, for a review of the current state of AGN jet research).

The central nuclear region can be resolved with very long baseline interferometry (VLBI) radio observations (see Boccardi et al. 2017, for a review). In images obtained from such observations, AGN often show a "core-jet" structure, with a bright feature referred to as the VLBI core, and a lower-intensity extended jet. The VLBI core corresponds to the synchrotron photosphere of the outgoing jet flow, that is, a transition between an optically thick inner region and an optically thin outer region. Thus, its location and properties depend on the observing frequency, with cores observed at higher frequencies approaching the central engine of the system ("core

Table 1. Summary of the EHT 2017 observations at 230 GHz.

Common	B1950	J2000	Redshift z	Type	Volume	Days (Apr. 2017)	Sites	BL (km)	Ref.
Sagittarius A*	1742–286	J1750–2900	–	–	23024	5, 6, 7, 10, 11	all	11204	(1)
3C 279	1253–055	J1256–0547	0.538	Q	9638	5, 6, 10, 11	all	11297	(2)
M 87	1228+126	J1230+1223	0.0042	R	8846	5, 6, 10, 11	all but Y	10835	(3)
OJ 287	0851+202	J0854+2006	0.306	B	4548	5, 10, 11	all but Y	10834	(4)
Centaurus A	1322–427	J1325-4303	0.0014	R	3218	10	all but P	10749	(5)
J1924–2914	1921–293	J1924–2914	0.353	Q	2937	5, 6, 7, 10, 11	all	11091	(6)
NRAO 530	1730–130	J1733–1304	0.902	Q	1439	5, 6, 7	all	11305	(7)
3C 273	1226+023	J1229+0203	0.158	Q	642	6	all but Y	9372	(8)
1749+096	1749+096	J1751+0939	0.322	B	612	10	J, L, S, X, Z	9342	
1055+018	1055+018	J1058+0133	0.89	Q	488	5, 10, 11	all but Y	8904	
BL Lacertae	2200+420	J2202+4216	0.069	B	174	7	J, S, X, Z	8934	
3C 84	0316+413	J0319+4130	0.0177	R	141	7	A, J, S, X, Z	9344	(9)
3C 454.3	2251+158	J2253+1608	0.859	Q	139	7	J, S, X	9382	
CTA 102	2230+114	J2232+1143	1.037	Q	118	7	J, S, X	9384	
J0132–1654	0130–171	J0132–1654	1.020	Q	65	6, 7	A, J, P, Y	11263	
J0006–0623	0003–066	J0006–0623	0.347	B	36	7	A, J, P, Y	11211	
NGC 1052	0238–084	J0241–0815	0.0049	R	20	6, 7	A, J, S, Y	5895	(10)
Cygnus X–3	2030+407	J2032+4057	–	X	16	5	J, S	<0.2	

Notes. The names listed in column "Common" follow the convention used by the EHT, and sometimes coincide with the "B1950" or "J2000" designations. Object types: B: BL Lac object; Q: quasar; R: radio galaxy; X: X-ray binary. Sites: A = ALMA; J = JCMT; L = LMT; P = PV; S = SMA; X = APEX; Y = SPT; Z = SMT. Redshifts taken from SIMBAD (Wenger et al. 2000); Sgr A* and Cyg X–3 are galactic sources. Volume: Total number of detections; BL: Maximum projected baseline. (1) The Event Horizon Telescope Collaboration (2022a); (2) Kim et al. (2020); (3) The Event Horizon Telescope Collaboration (2019a); (4) Gómez et al. in prep.; (5) Janssen et al. (2021); (6) Issaoun et al. (2022); (7) Jorstad et al. (2023); (8) Wielgus et al. (in prep.); (9) Paraschos et al. (2024); (10) Baczko et al. (2024).

shift", e.g., Pushkarev et al. 2012). This way, multifrequency radio-interferometric observations enable studies of the system's properties along the jet, constraining the energy contents of particles and magnetic fields, and indicating the acceleration mechanism.

The observing campaign of the Event Horizon Telescope (EHT) in April 2017 led to the first VLBI images of supermassive black holes (SMBHs). The primary event horizon scale science targets of the EHT were M 87* (The Event Horizon Telescope Collaboration 2019a,b,c,d,e,f, 2021a,b, 2023) and Sagittarius A* (The Event Horizon Telescope Collaboration 2022a,b,c,d,e,f, 2024a,b). Additionally, new results on several AGN were obtained: 3C 279 (Kim et al. 2020), Centaurus A (Janssen et al. 2021), J1924–2914 (Issaoun et al. 2022), NRAO 530 (Jorstad et al. 2023), 3C 84 (Paraschos et al. 2024), and NGC 1052 (Baczko et al. 2024). While the efforts to analyze individual EHT targets continue (Gómez et al., in prep.; Wielgus et al., in prep.), the first conclusions about the statistical properties of AGN sources at 230 GHz can be drawn, based on the EHT 2017 sample.

During the 2017 campaign, the EHT observed a total number of eighteen different sources, achieving detections on exceptionally long baselines (over $4.5\,\mathrm{G\lambda}$) for seventeen objects (see Table 1 for a summary of the observations). The set includes EHT collaboration projects (M 87 and Sgr A*), projects proposed by individual researchers (3C 279, OJ 287, Cen A, and others), along with all calibrator sources used (J1924–2914, NRAO 530, 3C 273, and others). While the (u, v) coverage for many of these sources is insufficient for imaging, as illustrated in Fig. 1, it is possible to estimate their angular size, brightness temperature, and fractional polarization. Such physical parameters are of particular importance to constrain theoretical models of accretion onto black holes

and outflows from their vicinity (e.g., Blandford & Königl 1979; Blandford & Payne 1982; Gabuzda et al. 2017, 2018; MacDonald & Marscher 2018; Kramer & MacDonald 2021; Cruz-Osorio et al. 2022; Fromm et al. 2022; Röder et al. 2023).

With this work, we inaugurate a 230 GHz catalog of sources that will grow with subsequent EHT campaigns. In particular, this work adds 230 GHz observations to the large existing sample of sources from surveys at lower frequencies. Since the mid 1990s, 86 GHz surveys have been carried out, first with the Coordinate Millimeter VLBI Array (CMVA; Rogers et al. 1995; Beasley et al. 1997; Rantakyro et al. 1998; Lonsdale et al. 1998; Lobanov et al. 2000; Lee et al. 2008), which was ultimately succeeded by the Global Millimeter VLBI Array (GMVA; Lee et al. 2008; Nair et al. 2019). Pushkarev & Kovalev (2012) carried out a survey at 2 GHz and 8 GHz using a combination of the Very Long Baseline Array (VLBA) and up to ten geodetic antennas. The long-running MOJAVE[1] (Kellermann et al. 2004; Lister & Homan 2005; Kovalev et al. 2005; Homan et al. 2006; Cohen et al. 2007; Lister et al. 2009, 2018, 2021) and VLBA-BU-BLAZAR/BEAM-ME[2] programs (Jorstad et al. 2017; Weaver et al. 2022) supply data at intermediate frequencies 15 GHz and 43 GHz, respectively, observed with the VLBA. Surveys at 5 GHz have been carried out with the VLBA in the frame of the VLBA imaging and polarimetry survey (VIPS; Helmboldt et al. 2007, 2008) and the VLBI space observatory program (VSOP; e.g., Dodson et al. 2008).

Characteristic properties of AGN jets may be revealed using a statistical approach to the investigation of the brightness temperature and its dependence on frequency, and in turn, on the distance from the central engine (Blandford & Königl 1979). Given a sufficiently large sample size, such an approach remains robust against uncertainties related to properties of individual

---

[1] Monitoring of jets in active galactic nuclei with VLBA experiments.
[2] Blazars entering the astrophysical multimessenger era.
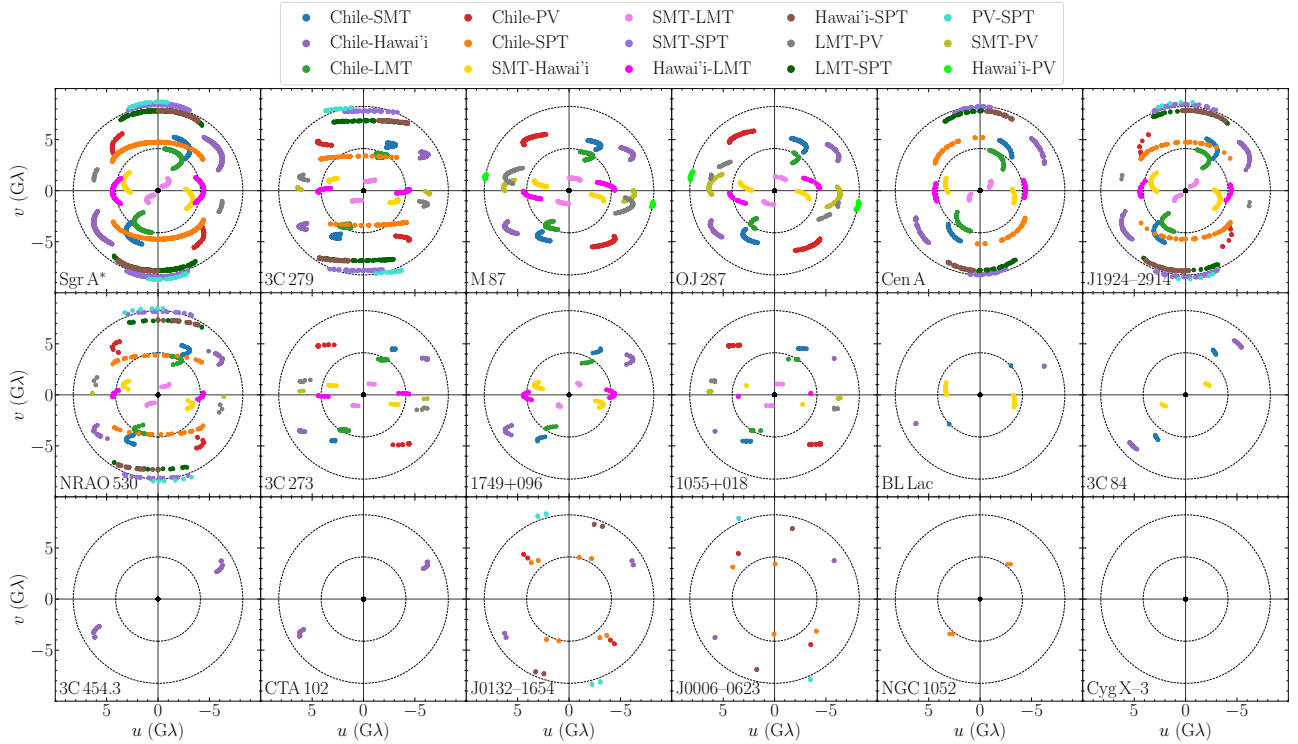
Fig. 1. (u, v) coverage for all sources observed during the EHT 2017 campaign, as summarized in Table 1, combining all available visibility detections for all days and bands, averaged in 120 s intervals. The two circles in each panel correspond to the fringe spacing characterizing an instrumental resolution of 25 and 50 μas. JCMT-SMA and ALMA-APEX are the very short intrasite baselines, shown as black data points near the origin of the (u, v) coordinate system (when available). JCMT and SMA are shown as "Hawai'i", while ALMA and APEX are shown as "Chile".

sources, such as poorly constrained inclination and bulk flow velocity, as long as errors are uncorrelated. Adding measurements at higher frequencies is expected to greatly enhance the results of such statistical analyses, extending the investigated jet region closer to the SMBH and thus allowing for more accurate tests of the inner jet models, including their launching (e.g., Blandford & Znajek 1977; Blandford & Payne 1982) and acceleration in the vicinity of the true central AGN engine (e.g., Blandford & Königl 1979; Marscher 1995; Heinz & Begelman 2000; Vlahakis & Königl 2004). Throughout this paper we adopt a cosmology with $H_0 = 67.7 \, \mathrm{km \, s^{-1} \, Mpc^{-1}}$, $\Omega_m = 0.307$, and $\Omega_\Lambda = 0.693$ (Planck Collaboration XIII 2016).

2. EHT results

2.1. EHT observations and data reduction

Eight facilities participated in the EHT observing campaign on April 5-11, 2017: The Atacama Large Millimeter/submillimeter Array (ALMA, A, operating as a phased array; Matthews et al. 2018; Goddi et al. 2019) and the Atacama Pathfinder Experiment (APEX, X) telescopes in Chile; the Large Millimeter Telescope Alfonso Serrano (LMT, L) in Mexico; the IRAM 30 m telescope (PV, P) in Spain; the Submillimeter Telescope (SMT, Z) in Arizona; the James Clerk Maxwell Telescope (JCMT, J) and the Submillimeter Array (SMA, S) in Hawai'i; and the South Pole Telescope (SPT, Y) in Antarctica. Two frequency bands, each 2 GHz wide, centered at 227.1 GHz (LO band) and 229.1 GHz (HI band) were recorded. For a detailed description of the EHT array instrumental configuration see The Event Horizon Telescope Collaboration (2019b).

Following correlation, the data were reduced using the EHT-HOPS (Blackburn et al. 2019) and rPICARD (Janssen

et al. 2019) pipelines to independently validate the results (The Event Horizon Telescope Collaboration 2019c). The EHT calibration procedures are described in detail in The Event Horizon Telescope Collaboration (2022b), with minor updates with respect to The Event Horizon Telescope Collaboration (2019c). Whenever applicable, polarization leakage was calibrated following The Event Horizon Telescope Collaboration (2021a) and Issaoun et al. (2022). The electric vector position angle (EVPA) calibration requires persistent participation of ALMA in the EHT observing array. As a consequence, the polarization leakage calibration could only be applied in a straightforward way to sources with coverage as good or better than that of 3C 273 (see Table 1 and Fig. 1, as well as Paraschos et al. 2024 for further details). In particular, the seven sources introduced in this paper (Table 1) were not calibrated for polarization leakage and the absolute EVPA. This issue has minimal impact on the total intensity analysis, but the polarimetric analysis is affected, see Appendix A. While EHT resolves structures on ∼10–500 μas angular scales, simultaneous ALMA-only measurements of flux densities and fractional polarization at 212–230 GHz at angular resolutions of ∼ 1 arcsec have been reported for a number of observed sources by Goddi et al. (2021), constraining the total flux density of the core and the compact jet.

2.2. EHT data sets and model fitting

A summary of the EHT observations in April 2017 is given in Table 1. The "Volume" column contains the number of scan-averaged detected visibilities (that is, time-averaged for several minutes, depending on a particular schedule, with separate polarimetric correlation products counted individually), indicating the relative constraining power of the respective data sets;

see also Fig. 1 for a comparison of the (u, v) coverage between the different EHT data sets. For Cygnus X–3 we only measured a short (intrasite) baseline flux density, preventing us from estimating source compactness. Apart from the two galactic sources (Sgr A* and Cyg X–3), the EHT data set contains observations of sixteen AGN sources, which are the subject of the analysis presented in this paper. For these sources we provide estimates of the black hole masses and Doppler factors in Appendix B.

Whenever a dedicated study of an individual EHT target is available ("Ref." column in Table 1), we used source parameters reported therein. For the remaining seven AGN sources with very sparse (u, v) coverage and with no dedicated analysis published, we performed geometric model fitting with linearly polarized circular Gaussian components using `eht-imaging` (Chael et al. 2016, 2022; Roelofs et al. 2023), exploiting heuristic optimization tools implemented in `SciPy` (Virtanen et al. 2020) to search for the best-fit solution. For each of these sources we used all available data (LO and HI bands, all available days) to constrain a single geometric model. The number of polarized circular Gaussian components was chosen based on the minimal number of the model degrees of freedom required to obtain a high quality fit to visibility amplitudes, closure phases, and fractional linear polarizations, generally characterized by the reduced χ-square $\chi_n^2 < 2$.

For five out of seven sources (1749+096, 1055+018, BL Lac, J0132–1654, J0006–0623) we modeled the morphology with two or three circular Gaussians, presented in Fig. 2. Low visibility amplitudes around ~1 Gλ for 1055+018 were identified as LMT miscalibration related to pointing issues (see also The Event Horizon Telescope Collaboration 2019c for a summary of issues with LMT in 2017). These points were downweighted for the amplitude fitting, but preserved for the closure phase fitting. For the other two out of seven sources (CTA 102 and 3C 454.3), a single circular Gaussian was sufficient to interpret the observations. We assume that the core components are nearly circularly symmetric.

In the cases of BL Lac (Casadio et al. 2021), 1055+018 (Weaver et al. 2022) and several other sources, the 230 GHz model fit structure is consistent with images obtained at lower frequencies. For other sources, the separation of scales between the highest angular resolution images available so far and our modeling results makes such a comparison difficult. In particular, we identify an east-west structure in 1749+096, well constrained by the data, but perpendicular to the jet observed at lower frequencies, extending in the north direction (Weaver et al. 2022). While in this paper we focus on the total intensity properties of the sources, we also obtained linear polarization results for the Gaussian components, reported in Appendix A (Fig. A.1) along with detailed parameters of the fitted Gaussian models (Table A.1) and more technical comments regarding the model fitting procedures.

The EHT measurements of the 230 GHz VLBI cores, discussed further in this work, can be represented on a plane of core brightness temperature (see Sect. 3.3) against isotropic spectral core luminosity $L_\nu \propto S_\nu D_L^2$ for the luminosity distance D_L, see Fig. 3. This representation emphasizes the differences between the types of observed sources within the inhomogeneous EHT data set, with radio galaxies at the lower luminosity and brightness temperature corner of the figure, and luminous, high brightness temperature quasars in the opposite corner. The figure does not show Sgr A*, with 230 GHz spectral luminosity $L_\nu \sim 10^{23}$ erg s^{-1} Hz^{-1}, over five orders of magnitude below the least luminous AGN in the sample.

3. Measurements in the EHT+ data set

We consider sixteen AGN sources observed by the EHT, as summarized in Tables 1 and 2. For this set of sources, we additionally use measurements obtained at lower frequencies. We refer to this collection of measurements as the EHT+ data set. The EHT+ data set below 230 GHz spans a range of frequencies from 2 to 86 GHz, taken from a variety of surveys and monitoring efforts. At 1.66, 4.84, and 22.24 GHz we used measurements from the RadioAstron space VLBI program (Kardashev et al. 2013; Kovalev et al. 2020; Kovalev et al., in prep.), comparing them to VLBA data at 2.3 GHz (single-epoch, Pushkarev & Kovalev 2012) and 24 GHz (multiepoch, de Witt et al. 2023), as well as measurements from the VSOP program at 5 GHz (Dodson et al. 2008). Further VLBA data include 8 GHz (Pushkarev & Kovalev 2012), 15 GHz (MOJAVE, Homan et al. 2021), and 43 GHz (VLBA-BU-BLAZAR, Weaver et al. 2022). At 86 GHz, we used results obtained in a single-epoch GMVA AGN survey (Lee et al. 2008). In addition to these survey results, we used core brightness temperature measurements for M 87 at 43 GHz (Cheng et al. 2020) and Centaurus A at 8.4 and 22.3 GHz (TANAMI[3], Müller et al. 2011). In order to increase the homogeneity of the data set and limit the impact of low resolution bias we exclude measurements obtained with arrays lacking long baselines, such as those procured using the Korean VLBI Network (KVN) for frequencies of 23, 43, 86, and 129 GHz (Lee et al. 2016b).

### 3.1. multifrequency power law fits

We aim to characterize the dependence of the measured quantities (VLBI core size, flux density, brightness temperature) on the frequency with a power law model. However, individual properties of sources differ, scaling the observables. These include their cosmological redshift, Doppler factor, intrinsic source power and distance, as well as their intrinsic variability. Hence, the scaling parameter b in a power law $b\nu^a$ is generally source-specific and the inhomogeneous data set may not be self-consistently fitted with a single power law. Thus, in this paper we treated the scaling b as a source-specific nuisance parameter and characterized the slope a for the EHT+ data set by studying 16 individual sources and subsequently aggregating the results. The parameter b absorbs effects impacting the observables for the individual sources as a constant (frequency-independent) factor, such as cosmological redshift, constant Doppler factor, or intrinsic power. It preserves the relative impact of effects depending on the frequency or location along the jet such as acceleration and energy conversion, which we studied here.

To evaluate the characteristic power law slope in a frequency dependence of a given quantity for the entire EHT+ sample, we considered a set of $N = 16$ slopes a_i, fitted separately for individual sources. We extracted their mean value m and standard deviation σ, and used $m \pm \sigma/\sqrt{N}$ as our estimate of the characteristic power law slope in the population. In Appendix B we further discussed this choice and compare it with alternative approaches, such as directly fitting all measurements with a single power law, demonstrating robustness of the estimated slopes.

3.2. Core size and flux density

We estimated the VLBI core diameter θ and flux density S_ν using geometric Gaussian model fitting (see Sect. 2.2), identi-

---

[3] Tracking active galactic nuclei with Austral milliarcsecond interferometry.
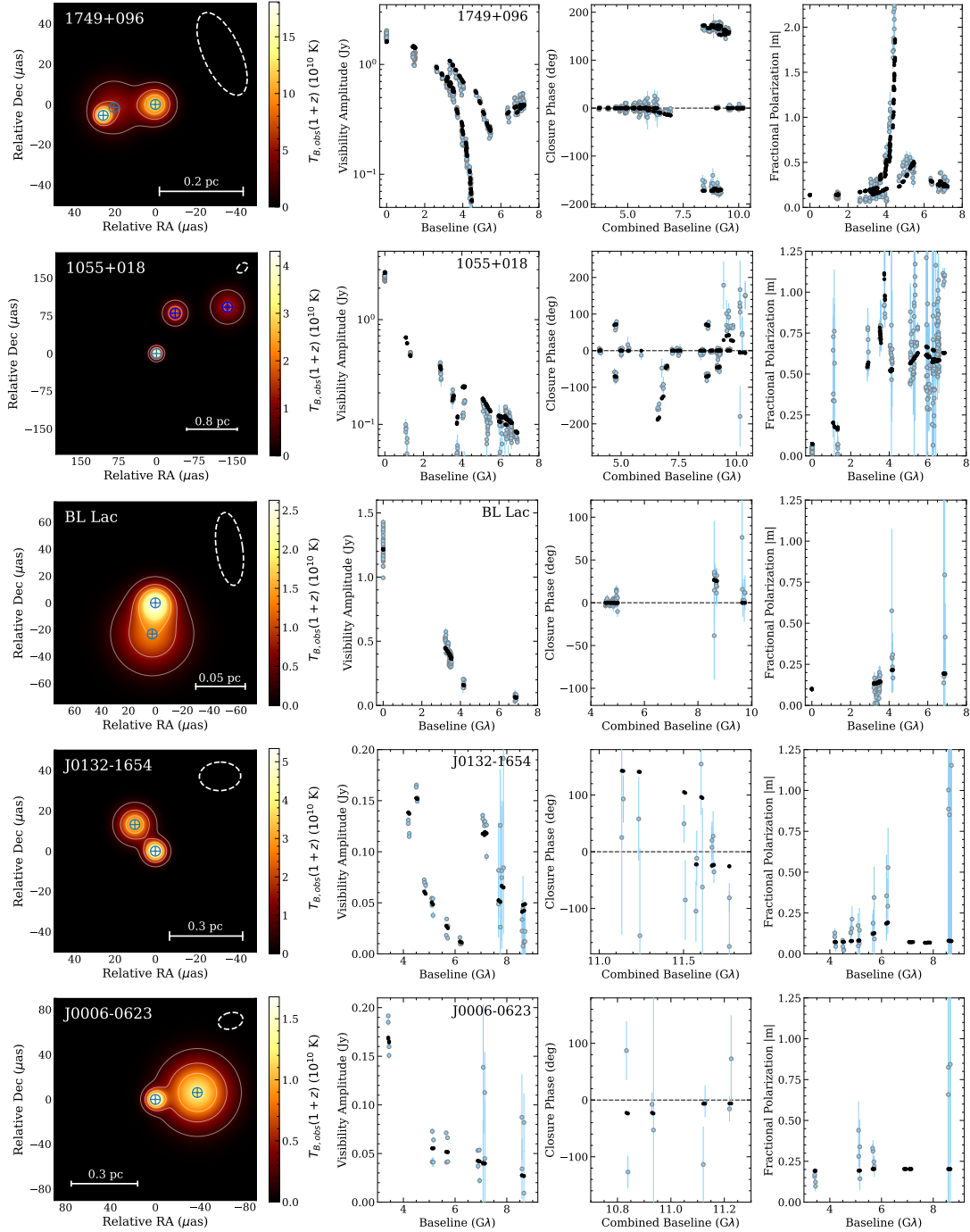
Fig. 2. Models of the EHT sources obtained through (polarized) circular Gaussian model fitting with at least two components. Blue crosses in the left column indicate positions of individual components. Contours represent 0.1, 0.3, 0.5, 0.7 and 0.9 of the peak total intensity. EHT observing beams are shown with dashed-line ellipses, to give a sense of the diffraction limited resolution supported by the data sets. We show consistency between models (black) and data (blue) for visibility amplitudes, closure phases, and absolute values of fractional visibility polarization. Closure phases are shown as a function of combined baseline length, which corresponds to a quadrature sum of lengths of all baselines from a given triangle. The visibility domain fractional polarization may exceed unity for resolved sources, such as is the case for 1749+096. The data shown contain detections only and no upper limits.

fying the core with the brightest of the fitted Gaussian components, that is, the component with the largest measured brightness temperature value. Both core size and core flux density parameters are generally subject to significant systematic uncertainties, related to the sparse (u, v) coverage. An interferometer is a spatial filter and the correlated flux density measured on the long baselines misses the resolved-out emission from structures larger than $\sim\lambda/BL$, where BL is the baseline length. This

effect should not negatively affect the characterization of the compact cores with the EHT, but may be relevant for extremely long baselines and lower observing frequencies, as is the case for the RadioAstron observations. Table 2 compares 230 GHz flux densities measured by the connected ALMA array ($\sim$100–300 kλ), the JCMT-SMA (J-S) baseline ($\sim$100 kλ), as well as the ALMA-APEX (A-X) baseline ($\sim$1.5 Mλ). There are indications of losses in VLBI flux density measurements in comparison with
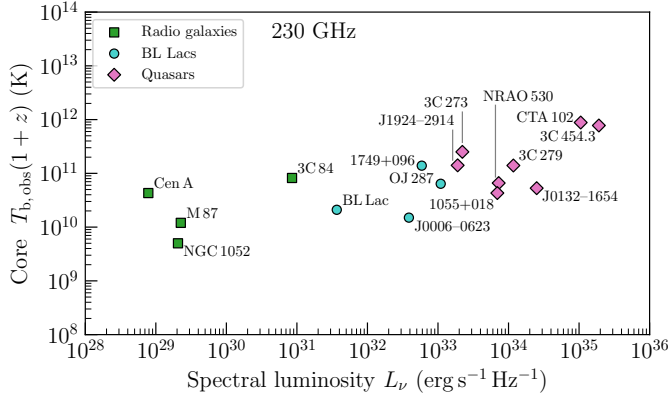
Fig. 3. Core brightness temperature against core synchrotron spectral luminosity for the EHT 2017 sample of 16 AGN sources. The sources cluster into categories of radio galaxies, BL Lacs (blazars), and quasars.

connected-element ALMA interferometry for comparable baseline lengths (see Appendix C). For the EHT data sets, ALMA flux densities can generally be considered to be the most reliable; thus, when available, they were used to calibrate the short VLBI baselines. This is the case in Table 2, where we give VLBI measurements for short intrasite baselines without scaling them to ALMA measurements, but the compact VLBI and core flux densities follow subsequent rescaling for sources with sufficient ALMA-only data (network calibration; Blackburn et al. 2019). Nonetheless, the additional flux density uncertainty of ~20% related to the ALMA-VLBI discrepancy (Appendix C) is subdominant with respect to other systematics and does not significantly impact our results.

In contrast to the flux density, the estimate of the core size may indeed be affected by the limited instrumental resolution. The configuration of the 2017 EHT array yields extreme angular resolution, but suffers from generally sparse coverage and lack of baselines probing milliarcsecond scales. Therefore, the dynamic range of the reconstructions is often low, and extended components are resolved out. Hence, studying jets on milliarcsecond and larger angular scales with the 2017 EHT array is effectively impossible. The array is, however, well suited for studying dominant, bright and compact core components in AGN systems. Indeed, none of the considered data sets shows clear indication of compact unresolved structures, though some of the lower frequency measurements in the EHT+ data set do – in those cases the core size estimates correspond to resolution-dependent upper limits.

The 15, 22, and 43 GHz measurements used in this analysis were respectively obtained from year- or decade-long surveys as parts of the MOJAVE program, the K-band celestial reference frame survey, and the VLBA-BU-BLAZAR/BEAM-ME programs. At higher frequencies, such monitoring programs are not available; 86 and 230 GHz measurements were collected in single-snapshot surveys. They may therefore not properly reflect the usual behavior of the individual variable sources. As an example, fluctuations of the 230 GHz compact ring-like core of M87 between 0.5 and 1.0 Jy were reported by Wielgus et al. (2020). The intrinsic source variability potentially contributes to uncertainty, if, for instance, a source happened to be in a flaring state during the observation. In the case of RadioAstron data, the correlation between increased source activity and availability of detections was addressed by treating the obtained brightness temperatures as upper limits.

Figure 4 shows the flux density and size of the VLBI cores in the EHT+ data set, as well as the resulting brightness temperatures, against frequency measured in the host frame of the AGN (corrected for the cosmological redshift, hereafter referred to simply as "host frame"). For 2, 5, and 22 GHz there are two sets of points, high angular resolution RadioAstron (semi-transparent markers) and lower resolution observations (solid-color markers). The systematic difference in the estimated core size is evident, with RadioAstron finding cores about an order of magnitude more compact. As a consequence, brightness temperatures inferred from RadioAstron observations sometimes approach 10^{14} K, which is difficult to reconcile with the assumption of incoherent synchrotron emission from relativistic electrons as it would require untypically high Doppler boosting (Kovalev et al. 2016). Another effect possibly limiting the accuracy of the obtained measurements, particularly at lower frequencies, is related to blending between the core and the foreground jet components.

In Fig. 4 we also present power law fits to ground array data from 15–230 GHz, that is, excluding the lower frequency measurements suffering from the aforementioned systematic shortcomings. The calculation of the power law slope follows the methodology described in Sect. 3.1. The spectra are almost flat (top panel), at most slightly decreasing with frequency as $S_\nu \sim \nu^{-0.4}$ for 15 GHz and above, as expected from VLBI cores at high observing frequencies. The estimated core size decreases as $\theta \sim \nu^{-0.6}$ in the range of 15–230 GHz. This decrease is less steep than the expected dependence dominated by the instrumental resolution effects $\sim \nu^{-1}$. The core size vs frequency panel of Fig. 4 indicates steepening of the slope at 2–8 GHz, in the region possibly more affected by the limited resolution and potentially also by scatter-broadening. This further justifies only selecting 15–230 GHz measurements for the power law fitting.

3.3. Brightness temperature

The brightness temperature T_b is an important tool to probe the nature and launching mechanisms of astrophysical jets. In the emitter frame, the intrinsic brightness temperature $T_{b, int}$ equals the equivalent black body temperature given the source surface brightness. It serves as a proxy of the temperature of electrons emitting the observed synchrotron radiation, enabling the characterization of the energy partition between plasma and the magnetic field, parametrized with the ratio of emitting particles energy to magnetic energy η assuming self-absorbed synchrotron radiation (Readhead 1994; Homan et al. 2006).

The observed $T_{b,obs}$ differs from the intrinsic value by a cosmological factor $(1 + z)^{-1}$ (usually known well) and the Doppler factor δ depending on the bulk outflow velocity and the jet viewing angle (usually known poorly),

$$T_{b, obs} = \frac{\delta}{1 + z} T_{b, int} = \frac{\delta}{1 + z} \eta^{2/17} T_{b, eq} = \frac{1}{1 + z} T_b, \qquad (1)$$

where $T_{b, eq} \approx 5 \times 10^{10}$ K is the equipartition brightness temperature (Readhead 1994). Following Eq. (1), in this work we denote the cosmological redshift-corrected brightness temperature (that is, measured in the frame of the host galaxy) simply with $T_b \equiv T_{b, obs}(1 + z) = \delta T_{b, int}$. For a circular Gaussian source model the peak brightness temperature in Kelvins can be calculated as

$$T_b = 1.22 \times 10^9 \left(\frac{S_\nu}{mJy}\right)\left(\frac{\nu}{GHz}\right)^{-2}\left(\frac{\theta}{mas}\right)^{-2}(1 + z)$$

$$= T_{b,obs}(1 + z), \qquad (2)$$

Table 2. Flux densities, core sizes, and core brightness temperatures at 230 GHz measured during the 2017 EHT observing campaign.

| Source | Flux Density (mJy) | | | | | Size | $T_{\mathrm{b,obs}}(1+z)$ | $T_{\mathrm{b,min}}(1+z)$ | $T_{\mathrm{b,lim}}(1+z)$ |
	ALMA [a]	J-S	A-X	compact	core	(μas)	$(10^{10}\,\mathrm{K})$	$(10^{10}\,\mathrm{K})$	$(10^{10}\,\mathrm{K})$
Sgr A*	2450 ± 250	1867 ± 312	1920 ± 140	2270	2270	53	1.4	1.1	1.2
3C 279	8800 ± 800	7050 ± 600	6510 ± 300	7890	2500	25	14.0	7.9	20.9
M 87	1310 ± 130	980 ± 133	920 ± 80	610	610	42	1.2	0.2	0.2
OJ 287	4270 ± 430	3085 ± 1100	2970 ± 230	3690	420	14	6.4	1.8	2.2
Cen A	5660 ± 570	4816 ± 367	4300 ± 120	1750	1750	30	4.3	2.0	3.3
J1924−2914	3200 ± 320	2472 ± 345	2550 ± 170	2470	500	11	14.1	19.7	78.9
NRAO 530	1590 ± 160	1248 ± 141	1140 ± 60	680	240	13.0	6.6	4.3	6.9
3C 273	7560 ± 760	6163 ± 700	5220 ± 210	6000	610	8.1	25.1	9.1	38.8
1749+096	–	1806 ± 135	–	1600	670	12.9	12.6	17.4	73.9
1055+018	3550 ± 400	2510 ± 140	2530 ± 120	1240	315	18.0	4.3	3.4	14.4
BL Lac	–	1241 ± 112	–	1220	1220	21.1	2.1	1.9	6.7
3C 84	–	9895 ± 321	7120 ± 440	1880	1040	17.5	8.2	6.8	29.0
3C 454.3	–	9126 ± 543	–	9040	9040	22.5	77.7	44.9	190.5
CTA 102	–	5475 ± 254	–	5400	5400	17.1	88.2	81.0	344.3
J0132−1654	415 ± 30	–	–	212	80	8.5	5.3	2.4	3.2
J0006−0623	1990 ± 200	–	–	930	91	13.9	1.5	2.4	3.9
NGC 1052	400 ± 50	350 ± 50	–	350	350	43.0	0.5	0.1	0.2
Cyg X–3 [b]	–	1770 ± 349	–	–	–	–	–	–	–

Notes. [a]Following Goddi et al. (2021), corresponding to ∼1 arcsec angular scale. [b]Measurements on April 6 and 7, 2017 with the IRAM 30m telescope at 228.7 GHz yielded respectively $S = (2.95 \pm 0.44)$ Jy and $S = (2.96 \pm 0.26)$ Jy (Krichbaum 2017). J-S: JCMT-SMA baseline (∼100 kλ or ∼1 arcsec); A-X: ALMA-APEX baseline (∼1.5 Mλ or ∼100 mas); compact: flux density constrained with long EHT baselines on a sub-mas scale.

where S_ν is the measured correlated flux density at the observing frequency ν, and θ is the angular size of the source, defined as the full width at half maximum (FWHM) of the fitted Gaussian. By using a simple Gaussian model, we neglect the transverse structure of the jet. The frequency in the host frame is larger than the one observed by a factor $(1 + z)$, but in the comoving frame of the emitting plasma it is reduced by a factor of δ, typically exceeding unity for jet sources.

Since modeling the source structure using sparse VLBI data is subject to large systematic uncertainties, model-agnostic estimates based solely on visibility measurements provide potentially useful limits on the brightness temperature (Lobanov 2015):

$$T_{\mathrm{b,min}} \approx 3.09 \left(\frac{\mathrm{BL}}{\mathrm{km}}\right)^2 \left(\frac{V_q}{\mathrm{mJy}}\right), \tag{3}$$

$$T_{\mathrm{b,lim}} \approx 1.14 \left(\frac{\mathrm{BL}}{\mathrm{km}}\right)^2 \left(\frac{V_q + \sigma_q}{\mathrm{mJy}}\right) \left(\ln \frac{V_q + \sigma_q}{V_q}\right)^{-1}, \tag{4}$$

with maximum baseline length BL, corresponding visibility amplitude V_q and its uncertainty σ_q. The values of BL are reported in Table 1; core component flux density, size, and peak brightness temperature of the source model $T_{\mathrm{b,obs}}(1+z)$, as well as the visibility-only brightness temperature estimates can be found in Table 2. The latter indicate broad consistency with the brightness temperatures obtained based on Gaussian component modeling.

In the case of sources with relatively good (u, v) coverage, with detailed analyses described in dedicated papers (e.g., Janssen et al. 2021; Gomez et al., in prep.), we report core parameters following the imaging results presented therein, without resorting to approximated geometric modeling with Gaussian components.

The resulting measurements of brightness temperature T_{b} are shown in the bottom panel of Fig. 4. The systematic difference

between measurements with long RadioAstron baselines (semi-transparent markers at 2, 5, and 22 GHz) and the other observations at the same frequencies obtained with the VLBA and as part of the VSOP program are clearly visible. A power law fit to the data at frequencies of 15 GHz and larger indicates a slope with an index of −0.95 ± 0.13, fitted with the methodology described in Sect. 3.1; see also the discussion in Appendix B.

4. Modeled quantities

4.1. Distance from the VLBI core to the black hole

We adopt the framework for relativistic jets established by Blandford & Königl (1979) and Königl (1981), assuming a supersonic, conical jet with an opening angle ϕ_o, and a viewing angle ι. We refer to this setup as the BK model. The jet bulk Lorentz factor γ_j is constant in this framework, and the jet magnetic field $B \propto r^{-m}$ and particle density $N \propto r^{-n}$ are described as functions of the distance r from the jet origin.

Following Lee et al. (2016a), we employ a measure for the distance of the observed VLBI core to the true central engine under the assumption of equipartition between the particles in the jet and the magnetic field. The VLBI core is defined as the region where the optical depth reaches unity. Then, the physical distance (measured along the jet) of the VLBI core to the true central engine is (Lobanov 1998):

$$r = \left(\frac{B_1^{k_\mathrm{b}}}{\nu(1+z)} \left[6.2 \times 10^{18} C_2(\alpha) \delta^\epsilon \phi_\mathrm{o} N_1\right]^{1/(\epsilon+1)}\right)^{1/k_\mathrm{r}} \mathrm{pc}, \tag{5}$$

where B_1 and N_1 are, respectively, the magnetic field strength and electron number density at $r_1 = 1$ pc distance from the jet origin, δ is the jet Doppler factor $\delta = (1 - \beta \cos \iota)^{-1} \gamma^{-1}$,
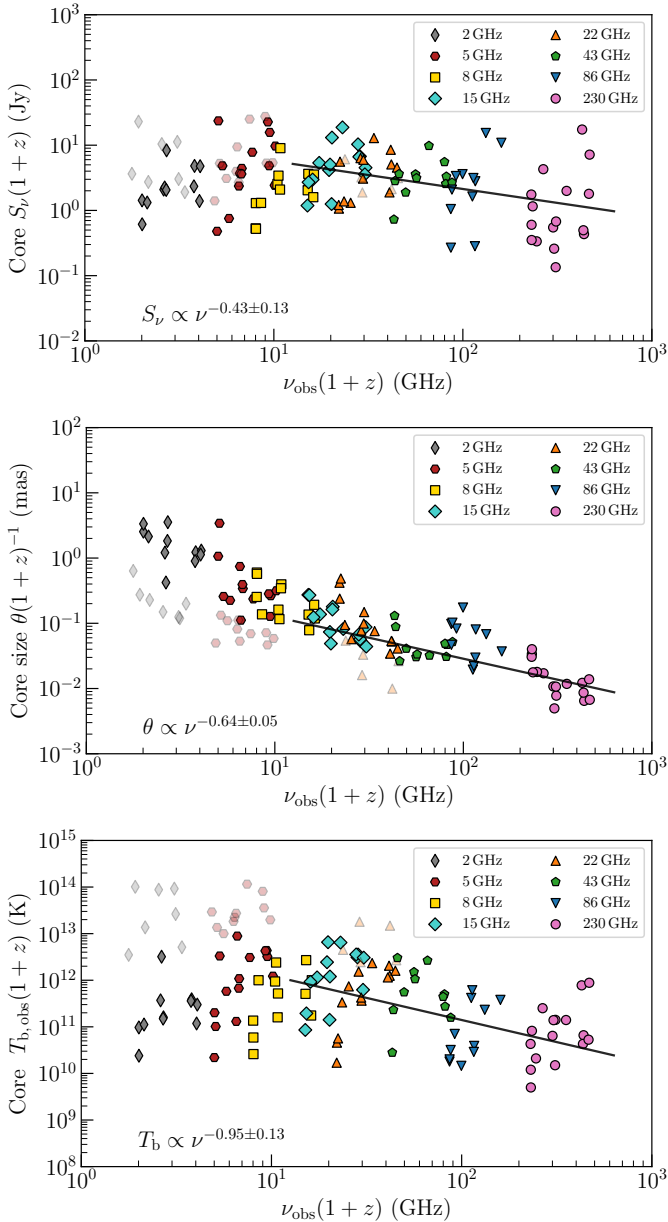
Fig. 4. Measurements of the core flux density (top), size (middle), and brightness temperature (bottom) obtained using the EHT+ data set of AGN sources, as a function of frequency in the host frame. The 15–230 GHz ground array data in each panel are approximated by power law fits (solid lines, obtained as detailed in Sect. 3.1) and the fit results are annotated. The faded data points are the RadioAstron measurements, while regular data points at the same frequencies correspond to VLBA and VSOP measurements; for comparability, we color the 1.66 GHz (L band) RadioAstron points the same as the 2 GHz (S band) VLBA points. The slope of the core flux density is shallow, $S_\nu \propto \nu^{-0.4}$. The core size decreases with frequency (and, in turn, increases with the distance from the central engine) as $\theta \propto \nu^{-0.6}$; the brightness temperature decreases with frequency as $T_b \propto \nu^{-1.0}$.

$C_2(-0.5) = 8.4 \times 10^{10}$ cgs (Pacholczyk 1970; Königl 1981) and

$$k_r = [(3 - 2\alpha)m + 2n - 2]/(5 - 2\alpha), \tag{6}$$

$$k_b = (3 - 2\alpha)/(5 - 2\alpha), \tag{7}$$

$$\epsilon = 3/2 - \alpha. \tag{8}$$

In this work we do not attempt to use Lorentz factors, Doppler factors, and viewing angles measured for individual sources.

Instead, following previous analyses, we assume a characteristic bulk Lorentz factor $\gamma_j = 10$ for the entire sample and $N_1 = 5 \times 10^3$ cm^{-3} at a distance of $r_1 = 1$ pc from the black hole (Lee et al. 2016a). For the intrinsic and observed opening angles, we set $\phi = 0.01$ rad $\approx 0.6°$ and $\phi_o = \phi \csc \iota$ with the viewing angle $\iota = 0.1$ rad, resulting in $\delta \approx 10$. Furthermore, following Königl (1981) and Lobanov (1998) we assume energy equipartition and adopt $m = 1$, $n = 2$, $k_r = 1$, $k_b = 2/3$, and $\epsilon = 2$, with $\alpha = -0.5$ ($S_\nu \propto \nu^\alpha$). The magnetic field strength B_1 at 1 pc can be expressed through the total synchrotron luminosity L_{syn}, following Blandford & Königl (1979):

$$L_{syn} = 4\pi D_L^2 S_{int} \propto \gamma_j^2 \beta_j c B_1^2 r_1^{2m} \phi^2, \tag{9}$$

where D_L is the luminosity distance to the source and S_{int} is the integrated, redshift corrected observed synchrotron flux density, integrated in the host frame frequency range between 1 GHz and 700 GHz by fitting a power law in ν to measured S_ν of each individual object. Equation (5) then takes a form

$$r = \left(\frac{K L_{syn}^{k_b/2}}{\nu(1+z)}\right)^{1/k_r} = \frac{K}{\nu(1+z)} L_{syn}^{1/3} \text{ pc}, \tag{10}$$

with a constant K incorporating the assumed BK model parameters. In order to correct L_{syn} for the Doppler effect, the right hand side of the Eq. (10) would be scaled by $\sim\delta^{-1}$, where the exact power depend on detailed physical assumptions (Ghisellini et al. 1993). The other Doppler factor present in Eq. (5) was absorbed into the K factor in Eq. (10) and for the assumed parameters corresponds to $\delta^{2/3}$, so the overall dependence of the radius estimate on the Doppler factor is shallow $\delta^{-1/3}$. In previous studies, the model described above was applied to measurements made at frequencies up to 86 GHz (Lee et al. 2016a; Nair et al. 2019).

The choice of particular fixed BK model jet parameters for an inhomogeneous sample of sources such as EHT+ is justified by the fact that the sample is dominated by quasars and BL Lac objects. Furthermore, we are mostly interested in the power law dependence. Essentially, with the methodology described in Sect. 3.1, the only BK model information impacting the power law index fits shown in Fig. 5 is that $r \sim \nu^{-1/k_r}$. We comment further on the impact of source-specific corrections in Appendix B, where we incorporate Doppler factor corrections following estimates given in Table B.2.

4.2. Magnetic field strength

The magnetic field strength of a synchrotron self-absorbed core can be roughly estimated as (e.g., Section 5.3 of Condon & Ransom 2016)

$$B \approx 1.4 \times 10^{21} \left(\frac{\nu_{obs}(1+z)}{\text{GHz}}\right) \left(\frac{T_{b,obs}(1+z)}{\text{K}}\right)^{-2} \text{ G}, \tag{11}$$

where we do not attempt to correct for the Doppler factor, which would increase B in the emitter's frame by a factor δ. While this estimate is independent of the BK jet model assumptions, it incorporates a very simplistic model for the emission spectrum. We found that Eq. (11), while having the same functional dependence of $B \propto \nu T_b^{-2}$, results in a magnetic field $\sim$25 times stronger compared to the B_{SSA} estimator of Marscher (1983) for identical input; the latter, however, is only applicable at the synchrotron turnover frequency. Hence, we expect a systematic upward bias of B. Nonetheless, the relative differences and the slopes remain useful for interpretation, provided that the VLBI cores do not become optically thin at the higher observing frequencies.
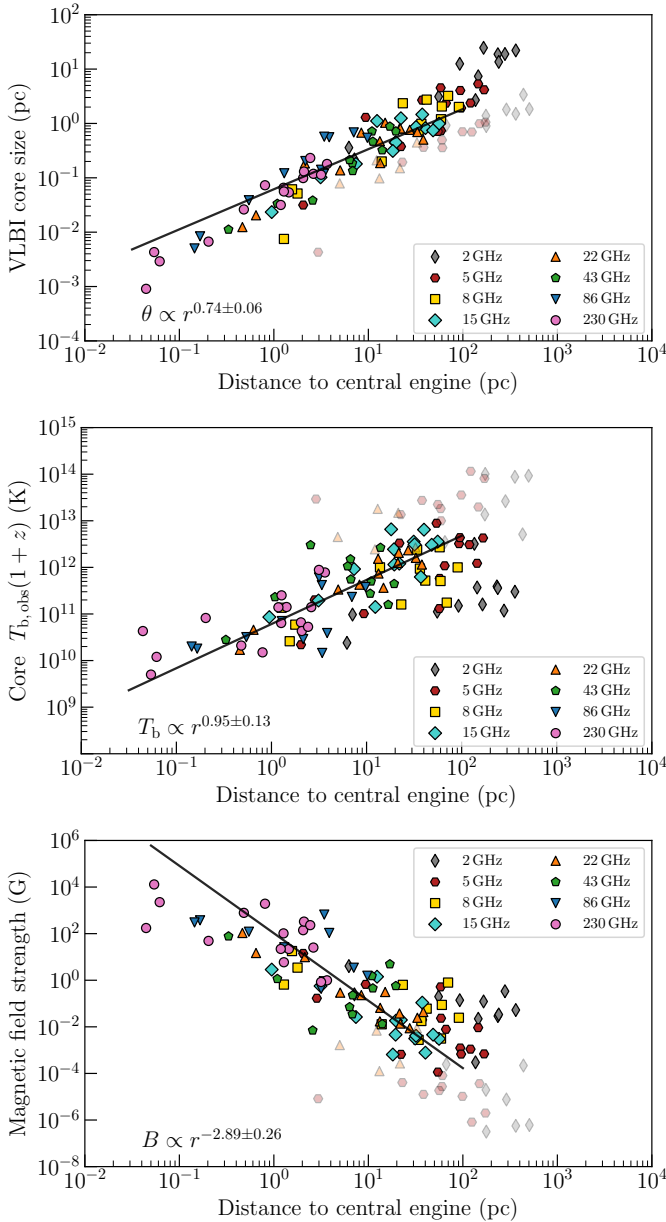
Fig. 5. Core size (top), brightness temperature (middle), and magnetic field estimate (bottom) obtained from the EHT+ data set as a function of the distance to the central engine. The 15–230 GHz data in each panel are approximated by power law fits (solid lines, obtained as detailed in Sect. 3.1) and the fit results are annotated. The faded data points at are the RadioAstron measurements, while the filled markers correspond to VLBA observations. For comparability, we color the 1.66 GHz (*L* band) RadioAstron points the same as the 2 GHz (*S* band) VLBA points. For a $M_\bullet = 10^8 M_\odot$ black hole 1 pc $= 2 \times 10^5 r_g$ with gravitational radius $r_g = GM_\bullet/c^2$.

5. Results and discussion

The observations collected in the EHT+ data set are presented in Fig. 4. In the framework of the BK jet model, we expect the intrinsic brightness temperature $T_{b, int}$ to not exceed the equipartition limit $T_{b, eq} \leq 10^{11}$ K (Readhead 1994; Lähteenmäki et al. 1999; Singal 2009) and, more fundamentally, the inverse Compton limit $T_{b, IC} \sim 5 \times 10^{11}$ K (Kellermann & Pauliny-Toth 1969; Nair et al. 2019). Observed brightness temperatures in excess of these limits may be caused by large Doppler factors as

$T_{b, obs}(1 + z) = \delta_{eq}T_{b, eq}$. The equipartition Doppler factors necessary to fulfill this condition are $\delta_{eq} < 10$ in the EHT sample at 230 GHz. Hence, from measured values of T_b alone, all sources are consistent with the equipartition limit without invoking unreasonably high Doppler factors at high observational frequencies. When interpreting brightness temperature measurements, we additionally make the crucial assumption that we observe self-absorbed, optically thick cores, and that they do not become fully optically thin at high observing frequencies.

In some cases, we observed 230 GHz brightness temperatures significantly below $T_{b, eq}$, which are better explained by a magnetically dominated inner jet, in which case the observed brightness temperature is reduced by $\eta^{2/17} < 1$, following Eq. (1). On the other hand, very large brightness temperatures obtained by RadioAstron at 1.7 and 5 GHz, reaching 10^{14} K, are difficult to reconcile with the assumption of equipartition, requiring unrealistically large equipartition Doppler factors. Instead, a more complicated core geometry or scattering sub-structure may play a role in driving up the brightness temperature (e.g., Johnson & Gwinn 2015; Johnson et al. 2016). The RadioAstron measurements were excluded from the power law fitting, which was limited to 15–230 GHz ground array data.

5.1. Tweaking the Blandford-Königl model parameters

The new observations at 230 GHz confirm that the brightness temperature T_b increases with the distance from the central engine, that is, it becomes larger for lower observing frequencies. Indications of such a trend were previously found by Lee et al. (2008) and Nair (2019). While quantifying these trends is hindered by significant systematic uncertainties, in Sect. 3 we reported the core size and brightness temperature dependence on the observing frequency $\theta \propto \nu^{-0.6}$ and $T_b \propto \nu^{-1.0}$.

To estimate the radial distance from the black hole to the VLBI core, we set up a jet model using various assumptions, as described in Sect. 4. For a conical BK jet, the core diameter scales with frequency as $\theta \propto r \propto \nu^{-1/k_r}$, where $k_r = 1$ in the case of equipartition. This immediate tension with the $\theta \propto \nu^{-0.6}$ dependence observed in Fig. 4 could be alleviated by a larger value of k_r. Following Eq. (6), k_r depends on the assumed radial density and magnetic field strength profiles; a larger k_r corresponds to a faster decay of these quantities with radius. In our example, changing $B \propto r^{-1}$ to $B \propto r^{-2}$ would be enough to reconcile the conical BK model with the observed relationship between core size and frequency. A steep decrease of the modeled magnetic field strength with radius is also found under the BK assumptions, see the bottom panel of Fig. 5 and Sect. 5.3.

Alternatively, the mismatch between our measurements and the brightness temperature, jet diameter and magnetic field strength radial dependence predicted by the BK model may be due to a transition from a parabolic to a conical jet geometry. There is ample observational evidence for a parabolic geometry of the jet base (e.g., Asada & Nakamura 2012; Hada et al. 2016, 2018; Okino et al. 2022; Ricci et al. 2022). Calculating the distances to the central engine using the BK model (Sect. 4 and Fig. 5), we find $\theta \propto r^{0.7}$, which deviates from the expectations for a conical jet ($\theta \propto r^{1.0}$) in the direction of a more parabolic structure ($\theta \propto r^{0.5}$). However, this predominantly shows the inconsistency of the canonical BK model with the data.

The brightness temperature is a derivative quantity of measured core size and flux density, $T_b \propto S_\nu \nu^{-2} \theta^{-2}$. For the canonical BK jet, S_ν is flat and $\theta \propto \nu^{-1}$, resulting in a flat T_b. From the EHT+ measurements we found a mildly negative slope of S_ν, and the slope of $\theta(\nu)$ is shallower than the BK prediction, adding up to the observed $T_b \propto \nu^{-1.0}$ dependence. While adjusting k_r, as discussed above, would take care of the impact of the core size

trend on T_b, it would not address the impact of the flux density trend.

5.2. Doppler factor evolution and energy conversion

Alternatively, the assumptions of a constant jet velocity or energy partition factor may need to be abandoned, as $T_b \propto \delta\eta^{2/17}$. With the power law slopes found in the bottom panel of Fig. 4 we obtain

$$T_{b,eq} = T_b\delta^{-1}\eta^{-2/17} \propto \nu_{int}^{-0.95}\delta^{-1.95}\eta^{-2/17}, \tag{12}$$

where $\nu_{int} = \nu_{obs}(1 + z)/\delta$ is the frequency in the emitter's frame. If we assume $\eta = $ const., we find a constant intrinsic brightness temperature for a physically reasonable $\delta \propto \nu_{int}^{-0.5} \propto r^{0.5}$ for $k_r = 1$. Hence, the Doppler factor grows more rapidly in the region close to the black hole. Allowing for η to increase with radius, as magnetic energy is transferred to particles, adds another degree of freedom and will generally decrease the slope of $\delta(r)$. If we additionally require a flat spectrum measured in the jet frame, given the observed S_ν slope (top panel of Fig. 4), we arrive at $\delta \propto r^{-0.3}$ and $\eta \propto r^{-3.1}$. These findings are a direct consequence of the observations and are independent of the BK model assumptions other than the choice of k_r with $\nu \propto r^{-k_r}$.

The growth of the Doppler factor with radius is a well motivated conclusion in the context of compact-scale AGN jets, since the bulk acceleration of the outflow must take place somewhere between the black hole and the parsec scales. A model in which both δ and η grow with radial distance from the black hole is consistent with a magnetically accelerated jet (Vlahakis & Königl 2004), transitioning from the magnetically (or Poynting) dominated innermost region to energy equipartition (or dominance of particle kinetic energy) further away. A different physical scenario has been proposed by Melia & Konigl (1989) and Marscher (1995), where an electron-positron jet is accelerated to ultra-relativistic energies at compact scales and subsequently decelerated through inverse-Compton scattering with external photons. In the process, high-energy emission in X-ray and γ-ray bands is produced, and the jet becomes progressively brighter in radio band further away from the black hole. This scenario was discussed in the context of the brightness temperature statistics by Lee (2014). We consider this model to be less physically plausible (see, e.g., Sikora et al. 1996, on the role of radiation drag for jet deceleration).

Another caveat is the possible impact of a change in viewing angle ι in a bending jet on the radial profile of the Doppler factor δ. Observations confirm the curved structure of some of the compact-scale jets in this work (e.g., Issaoun et al. 2022; Jorstad et al. 2023), further increasing the spread of brightness temperatures measured in the EHT+ sample with the viewing angle varying between the observing frequencies. If a certain source was bright at low frequencies due to a favorable viewing angle, it would show a lower core T_b than expected at higher frequencies, given a bend away from the favorable inclination in the more inner part of the jet. Moreover, an acceleration to speeds above $\beta = \upsilon/c = \cos\iota$ (or $\gamma > \csc\iota$) would decrease the observed T_b again, as the radiation becomes increasingly beamed along the jet axis, away from the observer at inclination ι. At large angular scales, we expect jets to be better described by the BK model, with a flat core spectrum $S_\nu(\nu)$, a continued high frequency trend in $\theta(\nu)$, and a flattening of $T_b(\nu)$. This seems to be the case for the 2 and 5 GHz observations shown in Fig. 4, although the conclusions are uncertain given the large spread and the small size of the sample.

5.3. Magnetic fields

The bottom panel of Fig. 5 shows the magnetic field estimates against the distance to the black hole, calculated with the BK model. For a canonical BK model (i.e., flat T_b), as described in Sect. 4, Eq. (11) gives $B \propto \nu \propto r^{-k_r}$, self-consistent assuming $m = k_r = 1$. However, since we measure $T_b \propto \nu^{-1}$, Eq. (11) gives $B \propto \nu^3 \propto r^{-3k_r}$, consistent with the result from fitting the data points in the bottom panel of Fig. 5. However, $3k_r = m$ would imply $m + n = 1$, requiring very shallow dependence of gas density and magnetic field strength with radius. These observations are thus in tension with the BK model. Correcting for the Doppler factor in Eqs. (10) and (11) would allow the steepness of the radial dependence of B to be mitigated.

Magnetic field estimates for the most compact scales reach $B \sim 10^3$ G, which is consistent with some predictions for magnetized accretion disks (Field & Rogers 1993). In the special case of M 87, where the central engine can be resolved, a correction for the over-estimation of the magnetic field (see Sect. 4.2) would bring down the obtained field strength to a value comparable to estimates made by the EHT in the previous studies (The Event Horizon Telescope Collaboration 2021b). Across the EHT+ sample the field strength decreases by about seven orders of magnitude toward the largest probed scales of $\sim10^6 r_g$ (~10 pc). At distances larger than one parsec estimated fields of $B \sim 10^{-4}$ G become comparable to the μG-field of the ambient medium (McKee & Ostriker 2007; Beck 2015). In the BK jet framework, the magnetic field components perpendicular and parallel to the jet axis behave as $B_\perp \propto r^{-1}$ (Blandford & Königl 1979) and $B_\parallel \propto r^{-2}$ (Königl 1981), respectively. We find that the $B(r)$ slope is steeper than -1, consistent with the steeper $B(r)$ slope inferred from the observed core size dependence on frequency. This supports the presence of poloidal (jet-parallel) magnetic fields in the inner jet regions, possibly forming a mixed helical geometry (Gabuzda et al. 2017). A steep decrease of the magnetic field strength with radius may also be indicative of an efficient conversion of magnetic energy into kinetic energy of particles through, for example, magnetic reconnection. The estimated slopes for some of the sources inspected individually are steeper than -3, following the decrease of the observed brightness temperature with frequency. This may be a consequence of rapid acceleration and a related radial increase of Doppler factor, unaccounted for in the BK model. Given the dependencies of $B_\parallel$ and $B_\perp$, a shallower slope in between -2 and -1 could be interpreted as a helical, but coherent field; the steep measured slope could hence indicate a loss of magnetic field coherence or strong dissipation through magnetic reconnection at larger distances. A steep slope of $B(r)$ could also indicate a decrease of the optical depth at high observing frequencies, biasing the magnetic field estimates upward in the more compact regions.

6. Summary and conclusions

In this work, we presented an analysis of the full EHT 2017 observational data set: the first 230 GHz VLBI campaign of this magnitude. We compiled the EHT+ sample of sixteen AGN sources observed by the EHT, along with their VLBI observations available at lower frequencies (2–86 GHz). For seven of these AGN sources we presented visibility domain modeling of the EHT data; the analyses of the remaining nine sources were given in separate papers. We first studied the change of the VLBI core flux density, size, and brightness temperature as a function of frequency in the EHT+ data set. Despite large scatter in the measurements, related to individual source properties, the joint

analysis reveals a shallow dependence of the core size on frequency $\theta \propto \nu^{-0.6}$ and a systematic decrease of the brightness temperature with frequency $T_b \propto \nu^{-1.0}$, indicating an increase of brightness temperature with the distance from the AGN central engine. These findings are qualitatively consistent with previous studies using lower and fewer observing frequencies.

We demonstrated that properties of AGN jet sources constrained by the VLBI observations at 15–230 GHz are incompatible with the standard BK model of a conical jet with constant Lorentz factor and energy partition. Discussing the impact of variations of the BK model parameters and the jet collimation profile led us to the conclusion that either a bulk acceleration of the jet (an increase of the Doppler factor with the jet radius), or a transfer of energy from the magnetic field to the emitting particles is required to interpret the data.

Both effects may occur simultaneously, and both are expected to play a role in compact scale jets based on theoretical models. A radial dependence of the Doppler factor $\delta \propto r^{0.5}$ (or a slightly shallower one, in the case of a radially evolving energy partition), could explain the observations. Our findings are consistent with these effects occurring gradually across the innermost parsec of the jet, or within $\sim 10^5\, r_g$ from the central black hole, with most of the Doppler factor increase occurring very close to the central engine.

Additionally, using the BK model, we estimated a steep decrease of magnetic field with radius $B \propto r^{-3}$, which is in tension with the underlying assumptions. The steepness of the slope may be reduced by incorporating a radially increasing Doppler factor, once again hinting at bulk acceleration of the jet. Alternatively, a strong dissipation of the magnetic energy may be taking place in the compact region of the AGN jets.

Subsequent EHT campaigns will deliver 230 GHz VLBI measurements for a larger number of objects, increasing our EHT+ sample size and thus its statistical robustness. With more high quality data it will become feasible to apply (possibly frequency dependent) Doppler corrections to individual sources. Further, studying jet kinematics on EHT scales through tracking of individual moving features and comparing these results with lower frequency VLBI data could conclusively demonstrate the radial profile of jet acceleration, breaking degeneracies in our theoretical models. Finally, an extension of VLBI capabilities to 345 GHz, which is already in the process of being implemented within the EHT, will provide insight on AGN jets on even more compact scales.

Data availability

A table compiling measured VLBI core flux densities, FWHM sizes and brightness temperatures, as well as the derived distances to the black hole, magnetic field strengths and synchrotron luminosities is available in electronic form at the CDS via anonymous ftp to `cdsarc.cds.unistra.fr` (`130.79.128.5`) or via `https://cdsarc.cds.unistra.fr/viz-bin/cat/J/A+A/695/A233`.

References

Agudo, I., Thum, C., Gómez, J. L., & Wiesemeyer, H. 2014, A&A, 566, A59
Asada, K., & Nakamura, M. 2012, ApJ, 745, L28
Baczko, A.-K., Kadler, M., Ros, E., et al. 2024, A&A, 692, A205
Beasley, A. J., Dhawan, V., Doeleman, S., & Phillips, R. B. 1997, in Millimeter-VLBI Science Workshop, eds. R. Barvainis, & R. B. Phillips, 53
Beck, R. 2015, A&A Rev., 24, 4
Blackburn, L., Chan, C.-K., Crew, G. B., et al. 2019, ApJ, 882, 23
Blandford, R. D., & Königl, A. 1979, ApJ, 232, 34
Blandford, R. D., & Payne, D. G. 1982, MNRAS, 199, 883
Blandford, R. D., & Znajek, R. L. 1977, MNRAS, 179, 433
Blandford, R., Meier, D., & Readhead, A. 2019, ARA&A, 57, 467
Boccardi, B., Krichbaum, T. P., Ros, E., & Zensus, J. A. 2017, A&A Rev., 25, 4
Casadio, C., MacDonald, N. R., Boccardi, B., et al. 2021, A&A, 649, A153
Chael, A. A., Johnson, M. D., Narayan, R., et al. 2016, ApJ, 829, 11
Chael, A., Chan, C. K., Bouman, K. L., et al. 2022, https://doi.org/10.5281/zenodo.7226661
Cheng, X. P., An, T., Frey, S., et al. 2020, ApJS, 247, 57
Cohen, M. H., Lister, M. L., Homan, D. C., et al. 2007, ApJ, 658, 232
Condon, J. J., & Ransom, S. M. 2016, Essential Radio Astronomy (Princeton University Press)
Cruz-Osorio, A., Fromm, C. M., Mizuno, Y., et al. 2022, Nat. Astron., 6, 103
de Witt, A., Jacobs, C. S., Gordon, D., et al. 2023, AJ, 165, 139
Dodson, R., Fomalont, E. B., Wiik, K., et al. 2008, ApJS, 175, 314
The Event Horizon Telescope Collaboration (Akiyama, K., et al.) 2019a, ApJ, 875, L1
The Event Horizon Telescope Collaboration (Akiyama, K., et al.) 2019b, ApJ, 875, L2
The Event Horizon Telescope Collaboration (Akiyama, K., et al.) 2019c, ApJ, 875, L3
The Event Horizon Telescope Collaboration (Akiyama, K., et al.) 2019d, ApJ, 875, L4
The Event Horizon Telescope Collaboration (Akiyama, K., et al.) 2019e, ApJ, 875, L5
The Event Horizon Telescope Collaboration (Akiyama, K., et al.) 2019f, ApJ, 875, L6
The Event Horizon Telescope Collaboration (Akiyama, K., et al.) 2021a, ApJ, 910, L12
The Event Horizon Telescope Collaboration (Akiyama, K., et al.) 2021b, ApJ, 910, L13
The Event Horizon Telescope Collaboration (Akiyama, K., et al.) 2022a, ApJ, 930, L12
The Event Horizon Telescope Collaboration (Akiyama, K., et al.) 2022b, ApJ, 930, L13
The Event Horizon Telescope Collaboration (Akiyama, K., et al.) 2022c, ApJ, 930, L14
The Event Horizon Telescope Collaboration (Akiyama, K., et al.) 2022d, ApJ, 930, L15
The Event Horizon Telescope Collaboration (Akiyama, K., et al.) 2022e, ApJ, 930, L16
The Event Horizon Telescope Collaboration (Akiyama, K., et al.) 2022f, ApJ, 930, L17
The Event Horizon Telescope Collaboration (Akiyama, K., et al.) 2023, ApJ, 957, L20
The Event Horizon Telescope Collaboration (Akiyama, K., et al.) 2024a, ApJ, 964, L25
The Event Horizon Telescope Collaboration (Akiyama, K., et al.) 2024b, ApJ, 964, L26
Field, G. B., & Rogers, R. D. 1993, ApJ, 403, 94
Fromm, C. M., Cruz-Osorio, A., Mizuno, Y., et al. 2022, A&A, 660, A107
Gabuzda, D. C., Roche, N., Kirwan, A., et al. 2017, MNRAS, 472, 1792
Gabuzda, D. C., Nagle, M., & Roche, N. 2018, A&A, 612, A67
Ghisellini, G., Padovani, P., Celotti, A., & Maraschi, L. 1993, ApJ, 407, 65
Goddi, C., Martí-Vidal, I., Messias, H., et al. 2019, PASP, 131, 075003
Goddi, C., Martí-Vidal, I., Messias, H., et al. 2021, ApJ, 910, L14
Hada, K., Kino, M., Doi, A., et al. 2016, ApJ, 817, 131
Hada, K., Doi, A., Wajima, K., et al. 2018, ApJ, 860, 141
Heinz, S., & Begelman, M. C. 2000, ApJ, 535, 104
Helmboldt, J. F., Taylor, G. B., Tremblay, S., et al. 2007, ApJ, 658, 203
Helmboldt, J. F., Taylor, G. B., Walker, R. C., & Blandford, R. D. 2008, ApJ, 681, 897
Homan, D. C., Kovalev, Y. Y., Lister, M. L., et al. 2006, ApJ, 642, L115
Homan, D. C., Cohen, M. H., Hovatta, T., et al. 2021, ApJ, 923, 67
Hovatta, T., Valtaoja, E., Tornikoski, M., & Lähteenmäki, A. 2009a, A&A, 494, 527
Hovatta, T., Valtaoja, E., Tornikoski, M., & Lähteenmäki, A. 2009b, A&A, 498, 723
Issaoun, S., Wielgus, M., Jorstad, S., et al. 2022, ApJ, 934, 145
Janssen, M., Goddi, C., van Bemmel, I. M., et al. 2019, A&A, 626, A75
Janssen, M., Falcke, H., Kadler, M., et al. 2021, Nat. Astron., 5, 1017
Johnson, M. D., & Gwinn, C. R. 2015, ApJ, 805, 180
Johnson, M. D., Kovalev, Y. Y., Gwinn, C. R., et al. 2016, ApJ, 820, L10
Jorstad, S. G., Marscher, A. P., Morozova, D. A., et al. 2017, ApJ, 846, 98
Jorstad, S., Wielgus, M., Lico, R., et al. 2023, ApJ, 943, 170
Kardashev, N. S., Khartov, V. V., Abramov, V. V., et al. 2013, Astron. Rep., 57, 153
Keck, M. L. 2019, Ph.D. Thesis, Boston University, USA
Kellermann, K. I., & Pauliny-Toth, I. I. K. 1969, ApJ, 155, L71

Kellermann, K. I., Lister, M. L., Homan, D. C., et al. 2004, ApJ, 609, 539
Kim, J.-Y., Krichbaum, T. P., Broderick, A. E., et al. 2020, A&A, 640, A69
Komossa, S., Grupe, D., Kraus, A., et al. 2023, MNRAS, 522, L84
Königl, A. 1981, ApJ, 243, 700
Kovalev, Y. Y., Kellermann, K. I., Lister, M. L., et al. 2005, AJ, 130, 2473
Kovalev, Y. Y., Kardashev, N. S., Kellermann, K. I., et al. 2016, ApJ, 820, L9
Kovalev, Y. Y., Kardashev, N. S., Sokolovsky, K. V., et al. 2020, Adv. Space Res., 65, 705
Kramer, J. A., & MacDonald, N. R. 2021, A&A, 656, A143
Krichbaum, T. 2017, ATel, 10257, 1
Lähteenmäki, A., Valtaoja, E., & Wiik, K. 1999, ApJ, 511, 112
Lee, S.-S. 2014, J. Korean Astron. Soc., 47, 303
Lee, S.-S., Lobanov, A. P., Krichbaum, T. P., et al. 2008, AJ, 136, 159
Lee, S.-S., Lobanov, A. P., Krichbaum, T. P., & Zensus, J. A. 2016a, ApJ, 826, 135
Lee, S.-S., Wajima, K., Algaba, J.-C., et al. 2016b, ApJS, 227, 8
Liodakis, I., Marchili, N., Angelakis, E., et al. 2017, MNRAS, 466, 4625
Lister, M. L., & Homan, D. C. 2005, AJ, 130, 1389
Lister, M. L., Cohen, M. H., Homan, D. C., et al. 2009, AJ, 138, 1874
Lister, M. L., Aller, M. F., Aller, H. D., et al. 2018, ApJS, 234, 12
Lister, M. L., Homan, D. C., Kellermann, K. I., et al. 2021, ApJ, 923, 30
Lobanov, A. P. 1998, A&A, 330, 79
Lobanov, A. 2015, A&A, 574, A84
Lobanov, A. P., Krichbaum, T. P., Graham, D. A., et al. 2000, A&A, 364, 391
Lonsdale, C. J., Doeleman, S. S., & Phillips, R. B. 1998, AJ, 116, 8
MacDonald, N. R., & Marscher, A. P. 2018, ApJ, 862, 58
Marscher, A. P. 1983, ApJ, 264, 296
Marscher, A. P. 1995, Proc. Nat. Acad. Sci., 92, 11439
Matthews, L. D., Crew, G. B., Doeleman, S. S., et al. 2018, PASP, 130, 015002
McKee, C. F., & Ostriker, E. C. 2007, ARA&A, 45, 565
Melia, F., & Konigl, A. 1989, ApJ, 340, 162
Müller, C., Kadler, M., Ojha, R., et al. 2011, A&A, 530, L11
Nair, D. G. 2019, Ph.D. Thesis, University of Cologne, Germany
Nair, D. G., Lobanov, A. P., Krichbaum, T. P., et al. 2019, A&A, 622, A92
Neumayer, N. 2010, PASA, 27, 449
Okino, H., Akiyama, K., Asada, K., et al. 2022, ApJ, 940, 65
Pacholczyk, A. G. 1970, Radio Astrophysics. Nonthermal Processes in Galactic and Extragalactic Sources, Series of Books in Astronomy and Astrophysics (San Francisco: Freeman)
Paraschos, G. F., Kim, J. Y., Wielgus, M., et al. 2024, A&A, 682, L3
Planck Collaboration XIII. 2016, A&A, 594, A13
Pordes, R., OSG Consortium, Petravick, D., et al. 2007, J. Phys. Conf. Ser., 78, 012057
Pushkarev, A. B., & Kovalev, Y. Y. 2012, A&A, 544, A34
Pushkarev, A. B., Hovatta, T., Kovalev, Y. Y., et al. 2012, A&A, 545, A113
Pushkarev, A. B., Kovalev, Y. Y., Lister, M. L., & Savolainen, T. 2017, MNRAS, 468, 4992
Rantakyro, F. T., Baath, L. B., Backer, D. C., et al. 1998, A&AS, 131, 451
Readhead, A. C. S. 1994, ApJ, 426, 51
Ricci, L., Boccardi, B., Nokhrina, E., et al. 2022, A&A, 664, A166
Röder, J., Cruz-Osorio, A., Fromm, C. M., et al. 2023, A&A, 671, A143
Roelofs, F., Johnson, M. D., Chael, A., et al. 2023, ApJ, 957, L21
Rogers, A. E. E., Phillips, R. B., & Lonsdale, C. J. 1995, Am. Astron. Soc. Meeting Abstr., 187, 12.12
Sfiligoi, I., Bradley, D. C., Holzman, B., et al. 2009, in 2009 WRI World Congress on Computer Science and Information Engineering, 2, 428
Sikora, M., Sol, H., Begelman, M. C., & Madejski, G. M. 1996, MNRAS, 280, 781
Singal, A. K. 2009, ApJ, 703, L109
Torrealba, C. J. A. 2012, Ph.D. Thesis, UNAM, Mexico
Torrealba, J., Chavushyan, V., Cruz-González, I., et al. 2012, Rev. Mex. Astron. Astrofis., 48, 9
Virtanen, P., Gommers, R., Oliphant, T. E., et al. 2020, Nat. Methods, 17, 261
Vlahakis, N., & Königl, A. 2004, ApJ, 605, 656
Weaver, Z. R., Jorstad, S. G., Marscher, A. P., et al. 2022, ApJS, 260, 12
Wenger, M., Ochsenbein, F., Egret, D., et al. 2000, A&AS, 143, 9
Wielgus, M., Akiyama, K., Blackburn, L., et al. 2020, ApJ, 901, 67
Woo, J.-H., & Urry, C. M. 2002, ApJ, 579, 530

[1] Max-Planck-Institut für Radioastronomie, Auf dem Hügel 69, D-53121 Bonn, Germany
[2] Instituto de Astrofísica de Andalucía-CSIC, Glorieta de la Astronomía s/n, E-18008 Granada, Spain
[3] Astronomy Department, Universidad de Concepción, Casilla 160-C, Concepción, Chile
[4] Korea Astronomy and Space Science Institute, Daedeok-daero 776, Yuseong-gu, Daejeon 34055, Republic of Korea
[5] Massachusetts Institute of Technology Haystack Observatory, 99 Millstone Road, Westford, MA 01886, USA
[6] Black Hole Initiative at Harvard University, 20 Garden Street, Cambridge, MA 02138, USA
[7] Center for Astrophysics | Harvard & Smithsonian, 60 Garden Street, Cambridge, MA 02138, USA
[8] Steward Observatory and Department of Astronomy, University of Arizona, 933 N. Cherry Ave., Tucson, AZ 85721, USA
[9] Data Science Institute, University of Arizona, 1230 N. Cherry Ave., Tucson, AZ 85721, USA
[10] Program in Applied Mathematics, University of Arizona, 617 N. Santa Rita, Tucson, AZ 85721, USA
[11] NASA Hubble Fellowship Program, Einstein Fellow, USA
[12] Department of Astrophysics, Institute for Mathematics, Astrophysics and Particle Physics (IMAPP), Radboud University, P.O. Box 9010, 6500 GL Nijmegen, The Netherlands
[13] Institute of Astronomy and Astrophysics, Academia Sinica, 645 N. A'ohoku Place, Hilo, HI 96720, USA
[14] Department of Physics and Astronomy, University of Hawaii at Manoa, 2505 Correa Road, Honolulu, HI 96822, USA
[15] Leiden Observatory, Leiden University, Postbus 2300, 9513, RA Leiden, The Netherlands
[16] Netherlands Organisation for Scientific Research (NWO),Postbus 93138, 2509 AC Den Haag, The Netherlands
[17] Aalto University Department of Electronics and Nanoengineering, PL 15500, FI-00076 Aalto, Finland
[18] Aalto University Metsähovi Radio Observatory, Metsähovintie 114, FI-02540 Kylmälä, Finland
[19] National Radio Astronomy Observatory, 520 Edgemont Road, Charlottesville, VA 22903, USA
[20] Department of Space, Earth and Environment, Chalmers University of Technology, Onsala Space Observatory, SE-43992 Onsala, Sweden
[21] Shanghai Astronomical Observatory, Chinese Academy of Sciences, 80 Nandan Road, Shanghai 200030, People's Republic of China
[22] Instituto de Astronomia, Geofísica e Ciências Atmosféricas, Universidade de São Paulo, R. do Matão, 1226, São Paulo, SP 05508-090, Brazil
[23] Dipartimento di Fisica, Universitá degli Studi di Cagliari, SP Monserrato-Sestu km 0.7, I-09042 Monserrato (CA), Italy
[24] INAF – Osservatorio Astronomico di Cagliari, via della Scienza 5, I-09047 Selargius (CA), Italy
[25] INFN, sezione di Cagliari, I-09042 Monserrato (CA), Italy
[26] Instituto de Física, Pontificia Universidad Católica de Valparaíso, Casilla 4059, Valparaíso, Chile
[27] Independent researcher
[28] Department of Astronomy, University of Illinois at Urbana-Champaign, 1002 West Green Street, Urbana, IL 61801, USA
[29] National Astronomical Observatory of Japan, 2-21-1 Osawa, Mitaka,Tokyo 181-8588, Japan
[30] Departament d'Astronomia i Astrofísica, Universitat de Valéncia, streetC. Dr. Moliner 50 E-46100 Burjassot, Valéncia, Spain
[31] Department of Physics, Faculty of Science, Universiti Malaya, 50603 Kuala Lumpur, Malaysia
[32] Department of Physics & Astronomy, The University of Texas at San Antonio, One UTSA Circle, San Antonio, TX 78249, USA
[33] Institute of Astronomy and Astrophysics, Academia Sinica, 11F of Astronomy-Mathematics Building, AS/NTU No. 1, Sec. 4, Roosevelt Rd., Taipei 106216, Taiwan, R.O.C.
[34] Observatori Astronómic, Universitat de Valéncia, C. Catedrático José Beltrán 2, E-46980 Paterna, Valéncia, Spain
[35] Yale Center for Astronomy & Astrophysics, Yale University, 52 Hillhouse Avenue, New Haven, CT 06511, USA
[36] Department of Physics, University of Illinois, 1110 West Green Street, Urbana, IL 61801, USA

[37] Fermi National Accelerator Laboratory, MS209, P.O. Box 500, Batavia, IL 60510, USA

[38] Department of Astronomy and Astrophysics, University of Chicago, 5640 South Ellis Avenue, Chicago, IL 60637, USA

[39] East Asian Observatory, 660 N. A'ohoku Place, Hilo, HI 96720, USA

[40] James Clerk Maxwell Telescope (JCMT), 660 N. A'ohoku Place, Hilo, HI 96720, USA

[41] California Institute of Technology, 1200 East California Boulevard, Pasadena, CA 91125, USA

[42] Institut de Radioastronomie Millimétrique (IRAM), 300 rue de la Piscine, F-38406 Saint Martin d'Hères, France

[43] Perimeter Institute for Theoretical Physics, 31 Caroline Street North, Waterloo ON N2L 2Y5, Canada

[44] Department of Physics and Astronomy, University of Waterloo, 200 University Avenue West, Waterloo ON N2L 3G1, Canada

[45] Waterloo Centre for Astrophysics, University of Waterloo, Waterloo ON N2L 3G1, Canada

[46] Department of Astronomy, University of Massachusetts, Amherst, MA 01003, USA

[47] University of Science and Technology, Gajeong-ro 217, Yuseong-gu, Daejeon 34113, Republic of Korea

[48] Kavli Institute for Cosmological Physics, University of Chicago, 5640 South Ellis Avenue, Chicago, IL 60637, USA

[49] Department of Physics, University of Chicago, 5720 South Ellis Avenue, Chicago, IL 60637, USA

[50] Enrico Fermi Institute, University of Chicago, 5640 South Ellis Avenue, Chicago, IL 60637, USA

[51] Princeton Gravity Initiative, Jadwin Hall, Princeton University, Princeton, NJ 08544, USA

[52] Cornell Center for Astrophysics and Planetary Science, Cornell University, Ithaca, NY 14853, USA

[53] Key Laboratory of Radio Astronomy and Technology, Chinese Academy of Sciences, A20 Datun Road, Chaoyang District Beijing 100101, People's Republic of China

[54] Department of Astronomy, Yonsei University, Yonsei-ro 50, Seodaemun-gu, 03722 Seoul, Republic of Korea

[55] Physics Department, Fairfield University, 1073 North Benson Road, Fairfield, CT 06824, USA

[56] Instituto de Astronomía, Universidad Nacional Autónoma de México (UNAM), Apdo Postal 70-264, Ciudad de México, Mexico

[57] Institut für Theoretische Physik, Goethe-Universität Frankfurt, Max-von-Laue-Straße 1, D-60438 Frankfurt am Main, Germany

[58] Research Center for Astronomical Computing, Zhejiang Laboratory, Hangzhou 311100, People's Republic of China

[59] Tsung-Dao Lee Institute, Shanghai Jiao Tong University, Shengrong Road 520, Shanghai 201210, People's Republic of China

[60] Department of Astronomy and Columbia Astrophysics Laboratory, Columbia University, 500 W. 120th Street, New York, NY 10027, USA

[61] Center for Computational Astrophysics, Flatiron Institute, 162 Fifth Avenue, New York, NY 10010, USA

[62] Dipartimento di Fisica "E. Pancini", Universitá di Napoli "Federico II", Compl. Univ. di Monte S. Angelo, Edificio G, Via Cinthia, I-80126 Napoli, Italy

[63] INFN Sez. di Napoli, Compl. Univ. di Monte S. Angelo, Edificio G, Via Cinthia, I-80126 Napoli, Italy

[64] Wits Centre for Astrophysics, University of the Witwatersrand, 1 Jan Smuts Avenue, Braamfontein, Johannesburg 2050, South Africa

[65] Department of Physics, University of Pretoria, Hatfield, Pretoria 0028, South Africa

[66] Centre for Radio Astronomy Techniques and Technologies, Department of Physics and Electronics, Rhodes University, Makhanda 6140, South Africa

[67] ASTRON, Oude Hoogeveensedijk 4, 7991 PD Dwingeloo, The Netherlands

[68] LESIA, Observatoire de Paris, Université PSL, CNRS, Sorbonne Université, Université de Paris, 5 place Jules Janssen, F-92195 Meudon, France

[69] JILA and Department of Astrophysical and Planetary Sciences, University of Colorado, Boulder, CO 80309, USA

[70] National Astronomical Observatories, Chinese Academy of Sciences, 20A Datun Road, Chaoyang District Beijing 100101, PR China

[71] Las Cumbres Observatory, 6740 Cortona Drive, Suite 102, Goleta, CA 93117-5575, USA

[72] Department of Physics, University of California, Santa Barbara, CA 93106-9530, USA

[73] Department of Electrical Engineering and Computer Science, Massachusetts Institute of Technology, 32-D476, 77 Massachusetts Ave., Cambridge, MA 02142, USA

[74] Google Research, 355 Main St., Cambridge, MA 02142, USA

[75] Institut für Theoretische Physik und Astrophysik, Julius-Maximilians-Universität Würzburg, Emil-Fischer-Straße 31, 97074 Würzburg, Germany

[76] Department of History of Science, Harvard University, Cambridge, MA 02138, USA

[77] Department of Physics, Harvard University, Cambridge, MA 02138, USA

[78] NCSA, University of Illinois, 1205 W. Clark St., Urbana, IL 61801, USA

[79] Institute for Mathematics and Interdisciplinary Center for Scientific Computing, Heidelberg University, Im Neuenheimer Feld 205, Heidelberg 69120, Germany

[80] Institut für Theoretische Physik, Universität Heidelberg, Philosophenweg 16, 69120 Heidelberg, Germany

[81] CP3-Origins, University of Southern Denmark, Campusvej 55, 5230 Odense, Denmark

[82] Instituto Nacional de Astrofísica, Óptica y Electrónica. Apartado Postal 51 y 216, 72000 Puebla Pue., Mexico

[83] Consejo Nacional de Humanidades, Ciencia y Tecnología, Av. Insurgentes Sur 1582, 03940 Ciudad de México, Mexico

[84] Key Laboratory for Research in Galaxies and Cosmology, Chinese Academy of Sciences, Shanghai 200030, People's Republic of China

[85] Mizusawa VLBI Observatory, National Astronomical Observatory of Japan, 2-12 Hoshigaoka, Mizusawa, Oshu, Iwate 023-0861, Japan

[86] Department of Astronomical Science, The Graduate University for Advanced Studies (SOKENDAI), 2-21-1 Osawa, Mitaka, Tokyo 181-8588, Japan

[87] Department of Physics, McGill University, 3600 rue University, Montréal QC H3A 2T8, Canada

[88] Trottier Space Institute at McGill, 3550 rue University, Montréal QC H3A 2A7, Canada

[89] NOVA Sub-mm Instrumentation Group, Kapteyn Astronomical Institute, University of Groningen, Landleven 12, 9747 AD Groningen, The Netherlands

[90] Department of Astronomy, School of Physics, Peking University, Beijing 100871, People's Republic of China

[91] Kavli Institute for Astronomy and Astrophysics, Peking University, Beijing 100871, People's Republic of China

[92] Department of Astronomy, Graduate School of Science, The University of Tokyo, 7-3-1 Hongo, Bunkyo-ku, Tokyo 113-0033, Japan

[93] The Institute of Statistical Mathematics, 10-3 Midori-cho, Tachikawa, Tokyo 190-8562, Japan

[94] Department of Statistical Science, The Graduate University for Advanced Studies (SOKENDAI), 10-3 Midori-cho, Tachikawa, Tokyo 190-8562, Japan

[95] Kavli Institute for the Physics and Mathematics of the Universe, The University of Tokyo, 5-1-5 Kashiwanoha, Kashiwa 277-8583, Japan

[96] ASTRAVEO LLC, PO Box 1668, Gloucester, MA 01931, USA

[97] Applied Materials Inc., 35 Dory Road, Gloucester, MA 01930, USA

[98] Institute for Astrophysical Research, Boston University, 725 Commonwealth Ave., Boston, MA 02215, USA

[99] Institute for Cosmic Ray Research, The University of Tokyo, 5-1-5 Kashiwanoha, Kashiwa, Chiba 277-8582, Japan

[100] Joint Institute for VLBI ERIC (JIVE), Oude Hoogeveensedijk 4, 7991 PD Dwingeloo, The Netherlands

[101] Department of Physics, Ulsan National Institute of Science and Technology (UNIST), 50 UNIST-gil, Eonyang-eup, Ulju-gun, Ulsan 44919, Republic of Korea

[102] Department of Physics, Korea Advanced Institute of Science and Technology (KAIST), 291 Daehak-ro, Yuseong-gu, Daejeon 34141, Republic of Korea

[103] Kogakuin University of Technology & Engineering, Academic Support Center, 2665-1 Nakano, Hachioji, Tokyo 192-0015, Japan

[104] Graduate School of Science and Technology, Niigata University, 8050 Ikarashi 2-no-cho, Nishi-ku, Niigata 950-2181, Japan

[105] Physics Department, National Sun Yat-Sen University, No. 70, Lien-Hai Road, Kaosiung City 80424, Taiwan, R.O.C.

[106] National Optical Astronomy Observatory, 950 N. Cherry Ave., Tucson, AZ 85719, USA

[107] Department of Physics, The Chinese University of Hong Kong, Shatin, N. T., Hong Kong

[108] School of Astronomy and Space Science, Nanjing University, Nanjing 210023, People's Republic of China

[109] Key Laboratory of Modern Astronomy and Astrophysics, Nanjing University, Nanjing 210023, People's Republic of China

[110] INAF-Istituto di Radioastronomia, Via P. Gobetti 101, I-40129 Bologna, Italy

[111] INAF-Istituto di Radioastronomia & Italian ALMA Regional Centre, Via P. Gobetti 101, I-40129 Bologna, Italy

[112] Department of Physics, National Taiwan University, No. 1, Sec. 4, Roosevelt Rd., Taipei 106216, Taiwan, R.O.C

[113] Instituto de Radioastronomía y Astrofísica, Universidad Nacional Autónoma de México, Morelia 58089, Mexico

[114] David Rockefeller Center for Latin American Studies, Harvard University, 1730 Cambridge Street, Cambridge, MA 02138, USA

[115] Yunnan Observatories, Chinese Academy of Sciences, 650011 Kunming, Yunnan Province, People's Republic of China

[116] Center for Astronomical Mega-Science, Chinese Academy of Sciences, 20A Datun Road, Chaoyang District, Beijing 100012, People's Republic of China

[117] Key Laboratory for the Structure and Evolution of Celestial Objects, Chinese Academy of Sciences, 650011 Kunming, People's Republic of China

[118] Anton Pannekoek Institute for Astronomy, University of Amsterdam, Science Park 904, 1098 XH Amsterdam, The Netherlands

[119] Gravitation and Astroparticle Physics Amsterdam (GRAPPA) Institute, University of Amsterdam, Science Park 904, 1098 XH Amsterdam, The Netherlands

[120] Department of Astrophysical Sciences, Peyton Hall, Princeton University, Princeton, NJ 08544, USA

[121] Science Support Office, Directorate of Science, European Space Research and Technology Centre (ESA/ESTEC), Keplerlaan 1, 2201 AZ Noordwijk, The Netherlands

[122] Department of Astronomy and Astrophysics, University of Chicago, Eckhardt, 5640 S Ellis Ave, Chicago, IL 60637, USA

[123] School of Physics and Astronomy, Shanghai Jiao Tong University, 800 Dongchuan Road, Shanghai 200240, People's Republic of China

[124] National Radio Astronomy Observatory, P.O. Box O, Socorro, NM 87801, USA

[125] Institut de Radioastronomie Millimétrique (IRAM), Avenida Divina Pastora 7, Local 20, E-18012 Granada, Spain

[126] National Institute of Technology, Hachinohe College, 16-1 Uwanotai, Tamonoki, Hachinohe City, Aomori 039-1192, Japan

[127] Research Center for Astronomy, Academy of Athens, Soranou Efessiou 4, 115 27 Athens, Greece

[128] Department of Physics, Villanova University, 800 Lancaster Avenue, Villanova, PA 19085, USA

[129] Physics Department, Washington University, CB 1105, St. Louis, MO 63130, USA

[130] Departamento de Matemática da Universidade de Aveiro and Centre for Research and Development in Mathematics and Applications (CIDMA), Campus de Santiago, 3810-193 Aveiro, Portugal

[131] School of Physics, Georgia Institute of Technology, 837 State St NW, Atlanta, GA 30332, USA

[132] School of Space Research, Kyung Hee University, 1732, Deogyeong-daero, Giheung-gu, Yongin-si, Gyeonggi-do 17104, Republic of Korea

[133] Canadian Institute for Theoretical Astrophysics, University of Toronto, 60 St. George Street, Toronto stateON M5S 3H8, Canada

[134] Dunlap Institute for Astronomy and Astrophysics, University of Toronto, 50 St. George Street, Toronto, ON M5S 3H4, Canada

[135] Canadian Institute for Advanced Research, 180 Dundas St West, Toronto, ON M5G 1Z8, Canada

[136] Radio Astronomy Laboratory, University of California, Berkeley, CA 94720, USA

[137] Institute of Astrophysics, Foundation for Research and Technology – Hellas, Voutes, 7110 Heraklion, Greece

[138] Dipartimento di Fisica, Universitá di Trieste, I-34127 Trieste, Italy

[139] INFN Sez. di Trieste, I-34127 Trieste, Italy

[140] Department of Physics, National Taiwan Normal University, No. 88, Sec. 4, Tingzhou Rd., Taipei 116, Taiwan, R.O.C.

[141] Center of Astronomy and Gravitation, National Taiwan Normal University, No. 88, Sec. 4, Tingzhou Road, Taipei 116, Taiwan, R.O.C.

[142] Finnish Centre for Astronomy with ESO, FI-20014 University of Turku, Finland

[143] Gemini Observatory/NSF NOIRLab, 670 N. A'ohōkū Place, Hilo, HI 96720, USA

[144] Department of Physics, University of Toronto, 60 St. George Street, Toronto, ON M5S 1A7, Canada

[145] Department of Physics, Tokyo Institute of Technology, 2-12-1 Ookayama, Meguro-ku, Tokyo 152-8551, Japan

[146] Hiroshima Astrophysical Science Center, Hiroshima University, 1-3-1 Kagamiyama, Higashi-Hiroshima, Hiroshima 739-8526, Japan

[147] Institut de Radioastronomie de Millimétrique (IRAM), 300 Rue de la Piscine, 38400 Saint-Martin-d'Hères, France

[148] Jeremiah Horrocks Institute, University of Central Lancashire, Preston PR1 2HE, UK

[149] National Biomedical Imaging Center, Peking University, Beijing 100871, People's Republic of China

[150] College of Future Technology, Peking University, Beijing 100871, People's Republic of China

[151] Department of Physics and Astronomy, University of Lethbridge, Lethbridge, Alberta T1K 3M4, Canada

[152] Department of Physics and Astronomy, Seoul National University, Gwanak-gu, Seoul 08826, Republic of Korea

[153] University of New Mexico, Department of Physics and Astronomy, Albuquerque, NM 87131, USA

[154] Physics Department, Brandeis University, 415 South Street, Waltham, MA 02453, USA

[155] Tuorla Observatory, Department of Physics and Astronomy, FI-20014 University of Turku, Finland

[156] Radboud Excellence Fellow of Radboud University, Nijmegen, The Netherlands

[157] School of Natural Sciences, Institute for Advanced Study, 1 Einstein Drive, Princeton, NJ 08540, USA

[158] School of Physics, Huazhong University of Science and Technology, Wuhan, Hubei430074, People's Republic of China

[159] Mullard Space Science Laboratory, University College London, Holmbury St. Mary, Dorking, Surrey RH5 6NT, UK

[160] Center for Astronomy and Astrophysics and Department of Physics, Fudan University, Shanghai 200438, People's Republic of China

[161] Astronomy Department, University of Science and Technology of China, Hefei 230026, People's Republic of China

[162] Department of Physics and Astronomy, Michigan State University, 567 Wilson Rd, East Lansing, MI 48824, USA

Appendix A: Models of the EHT sources

In Table A.1 we provide the results of geometric modeling for the seven sources observed during the EHT 2017 campaign that were not analysed in a separate publication. We considered circular Gaussian components with a constant fractional linear polarization. Our model-fitting procedure simultaneously minimizes errors on visibility amplitudes, closure phases, and fractional linear visibility polarization, see Section 2.2 and Fig. 2. We did not attempt to model circular polarization, given the very sparse sampling and low theoretically expected signal–to–noise ratio for the circular polarization. Furthermore, we did not generally fit for the amplitude gains, as they are very poorly constrained through interferometric closure quantities given such poor coverage. Instead, we incorporated ~ 10% gains uncertainty into the error budget for the visibility amplitudes. While for the EHT observations with sufficient coverage and ALMA participation we performed the calibration of the polarization leakage and the absolute electric vector position angle, this is not possible for the seven sources discussed here. Hence, in Table A.1 we only provide the absolute fractional polarization of each component, without the polarimetric position angle information. For the five sources modeled with more than one circular Gaussian we show the corresponding maps of the fractional polarization in Fig. A.1. In some cases (1749+096, 1055+018) we found extreme values of fractional polarization in the compact region. While the exact values are likely suffering from systematic biases related to sparse coverage and to a lack of the full polarization leakage calibration, the presence of high fractional polarization somewhere in the compact region appears to be a robust result following our detections of high polarized correlated flux density on long baselines. While the wide field of view observations of AGN jets indicate the increase of the fractional polarization with the observing frequency (Agudo et al. 2014), some of the values that we estimate strongly exceed theoretical expectations for the optically thick emission from a VLBI core. This is puzzling and may indicate issues with the reconstructed morphology of the polarized emission or a reduction of the optical depth at 230 GHz. The systematic uncertainties are difficult to quantify reliably, depending not only on the signal to noise ratio and the (u, v) coverage but also nontrivially on the uncertain underlying source structure. Hence, we refrain from reporting untrustworthy uncertainties in Table A.1. A conservative upper limit on the core brightness temperature uncertainty is a factor of two difference between the measurement and the true value.

Table A.1. Circular Gaussian models for the EHT 2017 sources

Source	Component	Flux (mJy)	FWHM (μas)	T_b (10^{10} K)	Distance (μas)	PA (deg)	p (%)
1749+096	Core	196	6.6	13.9	0	–	65
	Jet 1	744	20.4	5.5	6.6	−53.6	43
	Jet 2	674	12.9	12.6	26.4	−78.2	4.6
1055+018	Core	315	18.0	4.3	0	–	61
	Jet 1	531	34.8	1.9	88.1	−24.8	19
	Jet 2	850	52.5	1.4	168.0	−56.8	6.0
	Large scale	1108	–	–	–	–	3.6
BL Lac	Core	369	21.1	2.1	0	–	19
	Jet	848	40.9	1.3	23.2	+174.1	5.9
J0132−1654	Core	80	8.5	5.3	0	–	6.4
	Jet	132	13.2	3.6	16.6	+37.7	8.2
J0006−0623	Core	91	13.9	1.5	0	–	20
	Jet	834	46.3	1.2	37.9	−81.1	22
3C 454.3	Core	9040	22.5	77.7	0	–	17
CTA 102	Core	5400	17.1	88.2	0	–	12

Notes. PA: position angle with respect to the putative core (brightest component), east of north; p: fractional polarization of the component.
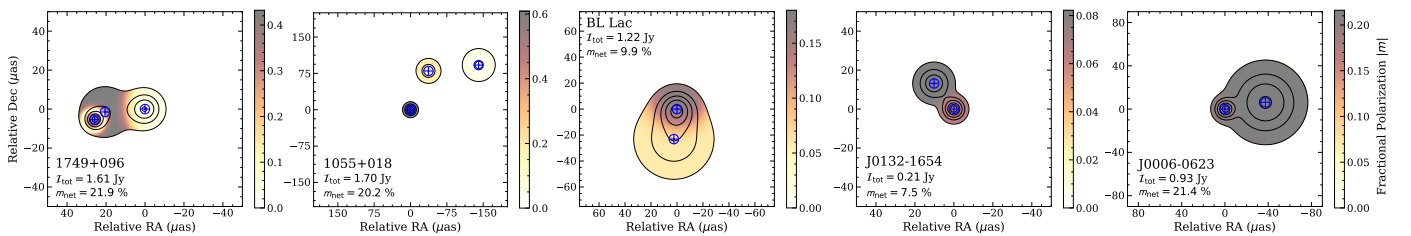
Fig. A.1. Models of the EHT 2017 sources obtained through the fitting of linearly polarized circular Gaussians. Contours represent 0.1, 0.3, 0.5, 0.7 and 0.9 of the peak total intensity brightness, same as in Fig. 2. Blue crosses: fitted positions of the Gaussians. Color map: fractional polarization. Total flux densities I_{tot} and total fractional polarization levels m_{net} for the reconstructed compact structures are annotated.

Appendix B: Doppler factor correction and power law fitting

Following Section 3.1, we used a dedicated procedure to characterize the dependence of observables with frequency using a power law model, while avoiding biases introduced by differences among individual sources, such as Doppler factor, intrinsic power, and distance. This procedure is labeled as "individual sources" in Table B.1, showing the same power law indices as reported in Section 3. This approach, while chosen as favorable, is not unique though. Importantly, the observational sensitivity itself introduces a bias limiting the spread of the observed flux density values. As long as this spread is subdominant with respect to the measured variation with frequency, a large sample in which uncorrelated biases of individual sources average out, may be studied with a single power law fit to all sources (Nair et al. 2019). In other words, this is equivalent to fitting directly to the multisource cloud of points in Fig. 4. We only account for the cosmological redshift correction, which is small and does not impact the fit significantly. The fitting results are shown in the column "cosmology only" in Table B.1, indicating a decent consistency with our default method. If we further attempt to correct for the Doppler factor using estimates aggregated in Table B.2, we increase the spread of points in the data as we act against the observational sensitivity bias that homogenized the observed flux densities. In other words, the spread grows as the data set is inhomogeneous in terms of the intrinsic (and not observed) source power. Thus, the fit to a Doppler-corrected cloud of multisource data becomes less consistent with the default method, see "Doppler correction" column in Table B.1. One may attempt to increase the homogeneity of the sample by restricting the analysis to quasars and BL Lacs, without radio galaxies ("Doppler, no radio galaxies" column in Table B.1). While this selection once again brings the estimated slopes to agreement with the default method, we neglect potentially useful data points. We conclude that our method based on aggregating power law fits to individual sources, insensitive to source-specific constant scaling such as cosmological redshift or frequency-independent Doppler factor, is the preferable fitting approach.

Table B.1. Slopes of the power law fits obtained with different methods of fitting to data shown in Fig. 4

quantity	cosmology only	Doppler correction	Doppler, no radio galaxies	individual sources
flux density S_ν	-0.43 ± 0.13	-0.01 ± 0.09	-0.48 ± 0.11	-0.43 ± 0.13
core size θ	-0.80 ± 0.07	-0.72 ± 0.04	-0.77 ± 0.06	-0.64 ± 0.05
brightness temperature T_b	-0.96 ± 0.16	-0.46 ± 0.10	-0.93 ± 0.13	-0.95 ± 0.13

Notes. Cosmology only: fits to the whole ensemble, corrected only for cosmological redshift; Doppler correction: Doppler correction applied to the data following Table B.2; Doppler, no radio galaxies: same as the previous column, but excluding radio galaxies; individual sources: Mean of fit results to individual sources with the procedure described in Section 3.1, shown as power laws in Fig. 4.

In Table B.2 we compiled the estimates of black hole masses and Doppler factors for the EHT+ sample of AGN sources. Both are subject to large systematic uncertainties. For sources without a black hole mass estimate we assumed $M_\bullet = 10^8 \, M_\odot$. For the Doppler factor corrections, we used values obtained from variability measurements at 15 GHz (Hovatta et al. 2009a,b; Liodakis et al. 2017, compiled in Pushkarev et al. 2017), filling the gaps with 43 GHz measurements from kinematics of characteristic jet components (Weaver et al. 2022). These measurements may not be of high accuracy, as the multifrequency light curve variability of radio flares is not necessarily representative of the underlying jet kinematics, and the choice of a "characteristic" jet component is rather arbitrary. For the remaining sources we assumed $\delta = 1$ for radio galaxies and $\delta = 10$ for quasars and BL Lacs.

Table B.2. Estimates for black hole mass and Doppler factor in the EHT+ AGN sample

Name	$M_\bullet$ ($10^8 \, M_\odot$)	Ref.	δ	Ref.	Name	$M_\bullet$ ($10^8 \, M_\odot$)	Ref.	δ	Ref.
3C 279	2.47 ± 0.26^a	1	23.8	7	M 87	65.0 ± 2.0^b	2	1.0	–
OJ 287	$\sim 1.0^c$	3	16.8	7	Cen A	0.55 ± 0.30^d	4	1.0	–
J1924–2914	1	–	10.0	–	NRAO 530	$\sim 3.0^e$	5	10.6	7
3C 273	7.83 ± 2.50^a	1	16.8	7	1749+096	1	–	11.9	7
1055+018	7.90 ± 0.36^a	1	12.1	7	BL Lac	$\sim 1.7^f$	6	7.2	7
3C 84	$\sim 3.0^f$	6	6.9	8	3C 454.3	12.17 ± 2.38^a	1	32.9	8
CTA 102	6.39 ± 0.24^a	1	15.5	8	J0132–1654	1	–	10.0	–
J0006–0623	1	–	5.1	7	NGC 1052	$\sim 1.55^f$	6	0.3	7

Notes. [a]spectral line widths [b]direct observation [c]scaling relations [d]stellar dynamics [e]spectral fitting [f]stellar velocity dispersion Doppler factors are estimated from 15 GHz variability (7 & refs. therein) or 43 GHz kinematics (8). If a source is not available in (7), the measurement is taken from (8). We assumed a Doppler factor $\delta = 1$ for the remaining radio galaxies (M 87 and Cen A), and $\delta = 10$ for the remaining quasars (J1924–2914 and J0006–0623).

References. (1) Torrealba (2012), Torrealba et al. (2012); (2) The Event Horizon Telescope Collaboration (2019a); (3) Komossa et al. (2023); (4) Neumayer (2010); (5) Keck (2019); (6) Woo & Urry (2002); (7) Pushkarev et al. (2017); (8) Weaver et al. (2022)

Appendix C: The flux density bias in the EHT VLBI data

We identify a systematic flux density deficit of 25% between short intra-site VLBI baselines and the ALMA-only connected interferometric array measurements (Goddi et al. 2021) after correcting for 7% ALMA VLBI losses (G. Crew, private communication). This bias, illustrated in Fig. C.1, is generally avoided in the EHT calibration framework through the network calibration procedure (The Event Horizon Telescope Collaboration 2019c; Blackburn et al. 2019; The Event Horizon Telescope Collaboration 2022b), scaling VLBI flux densities on intra-site baselines to ALMA measurements, whenever latter are available, through station-based amplitude gain calibration.

Further investigations are necessary to pin down the exact cause of this effect. For the sources without ALMA-only data available, such as the very sparse observations discussed in this paper, this bias is likely present, affecting the flux density measurements. We decided not to correct for this effect in case of sources modeled in this paper, as it is a) poorly characterized and it remains unclear if it affects all baselines in a uniform way, and b) because a bias of $\sim 20\%$ is of little importance for our order of magnitude considerations, which are dominated by other systematic uncertainties.
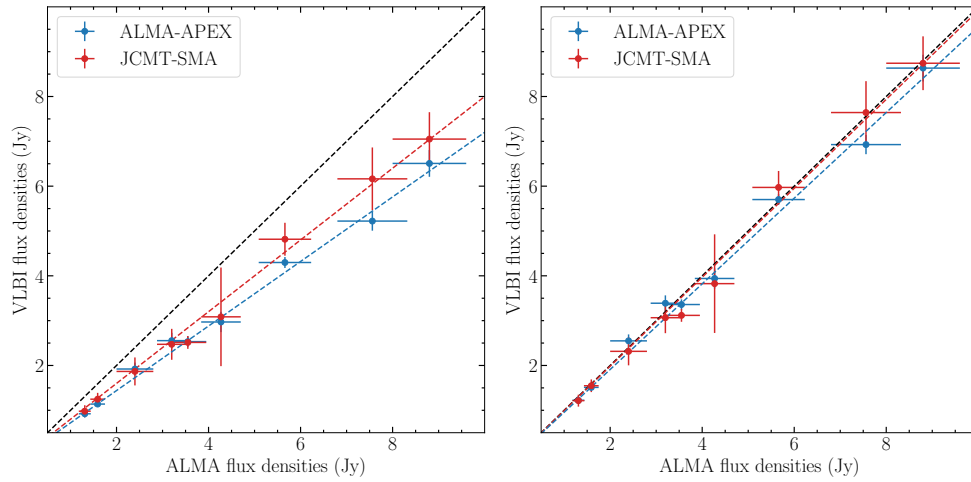
Fig. C.1. ALMA-only flux density measurements (Goddi et al. 2021) versus intra-site VLBI flux densities obtained during the EHT campaign, as reported in Table 2. The available data points correspond to observations of 3C279, 3C273, Centaurus A, OJ287, 1055+018, J1924-2914, Sgr A*, NRAO 530, and M87. Left panel: the dashed lines scale ALMA-only flux densities down by 0.8 (red) and 0.72 (blue), to approximately match ALMA-APEX and JCMT-SMA measurements. Right panel: after correcting for 7% ALMA VLBI losses and scaling all VLBI flux densities up by 25%, we find consistency with ALMA-only data for all the sources.

Appendix D: Acknowledgements